

## Article

# Slow Magnetic Relaxation in $\{[\text{CoCxAPy}]\cdot 2.15\text{H}_2\text{O}\}_n$ MOF Built from Ladder-Structured 2D Layers with Dimeric SMM Rungs

Ana Arauzo <sup>1,\*</sup>, Elena Bartolomé <sup>2</sup>, Javier Luzón <sup>1,3</sup>, Pablo J. Alonso <sup>1</sup>, Angelica Vlad <sup>4</sup>, Maria Cazacu <sup>4</sup>, Mirela F. Zaltariov <sup>4</sup>, Sergiu Shova <sup>4</sup>, Juan Bartolomé <sup>1</sup> and Constantin Turta <sup>4,5,†</sup>

<sup>1</sup> Instituto de Nanociencia y Materiales de Aragón (INMA), CSIC-Universidad de Zaragoza, Pedro Cerbuna 12, 50009 Zaragoza, Spain; jluzon@unizar.es (J.L.); alonso@unizar.es (P.J.A.); barto@unizar.es (J.B.)

<sup>2</sup> Department of Mechanical Engineering, Escola Universitària Salesiana de Sarrià (EUSS), Passeig de Sant Joan Bosco, 74, 08017 Barcelona, Spain; ebartolome@euss.es

<sup>3</sup> Centro Universitario de la Defensa, Ctra. de Huesca s/n, 50090 Zaragoza, Spain

<sup>4</sup> Department of Inorganic Polymers, “Petru Poni” Institute of Macromolecular Chemistry, Aleea Gr. Ghica Voda 41A, 700487 Iasi, Romania; avlad@icmpp.ro (A.V.); mcazacu@icmpp.ro (M.C.); zaltariov.mirela@icmpp.ro (M.F.Z.); shova@icmpp.ro (S.S.)

<sup>5</sup> Institute of Chemistry, Academy of Sciences of Moldova, Academiei 3, MD-2028 Chisinau, Moldova

\* Correspondence: aarauzo@unizar.es

† Constantin Turta passed away on 23 March 2015.



**Citation:** Arauzo, A.; Bartolomé, E.; Luzón, J.; Alonso, P.J.; Vlad, A.; Cazacu, M.; Zaltariov, M.F.; Shova, S.; Bartolomé, J.; Turta, C. Slow Magnetic Relaxation in  $\{[\text{CoCxAPy}]\cdot 2.15\text{H}_2\text{O}\}_n$  MOF Built from Ladder-Structured 2D Layers with Dimeric SMM Rungs. *Molecules* **2021**, *26*, 5626. <https://doi.org/10.3390/molecules26185626>

Academic Editors: Raed Abu-Reziq and Dawid Pinkowicz

Received: 21 June 2021

Accepted: 10 September 2021

Published: 16 September 2021

**Publisher’s Note:** MDPI stays neutral with regard to jurisdictional claims in published maps and institutional affiliations.



**Copyright:** © 2021 by the authors. Licensee MDPI, Basel, Switzerland. This article is an open access article distributed under the terms and conditions of the Creative Commons Attribution (CC BY) license (<https://creativecommons.org/licenses/by/4.0/>).

**Abstract:** We present the magnetic properties of the metal-organic framework  $\{[\text{CoCxAPy}]\cdot 2.15\text{H}_2\text{O}\}_n$  (Cx = bis(carboxypropyl)tetramethyldisiloxane; APy = 4,4'-azopyridine) (1) that builds up from the stacking of 2D coordination polymers. The 2D-coordination polymer in the *bc* plane is formed by the adjacent bonding of  $[\text{CoCxAPy}]$  1D two-leg ladders with Co dimer rungs, running parallel to the *c*-axis. The crystal packing of 2D layers shows the presence of infinite channels running along the *c* crystallographic axis, which accommodate the disordered solvate molecules. The Co(II) is six-coordinated in a distorted octahedral geometry, where the equatorial plane is occupied by four carboxylate oxygen atoms. Two nitrogen atoms from APy ligands are coordinated in apical positions. The single-ion magnetic anisotropy has been determined by low temperature EPR and magnetization measurements on an isostructural compound  $\{[\text{Zn}_{0.8}\text{Co}_{0.2}\text{CxAPy}]\cdot 1.5\text{CH}_3\text{OH}\}_n$  (2). The results show that the Co(II) ion has orthorhombic anisotropy with the hard-axis direction in the  $C_{2v}$  main axis, lying the easy axis in the distorted octahedron equatorial plane, as predicted by the *ab initio* calculations of the *g*-tensor. Magnetic and heat capacity properties at very low temperatures are rationalized within a  $S^* = 1/2$  magnetic dimer model with anisotropic antiferromagnetic interaction. The magnetic dimer exhibits slow relaxation of the magnetization (SMM) below 6 K in applied field, with a  $\tau_f \approx 2$  s direct process at low frequencies, and an Orbach process at higher frequencies with  $U/k_B = 6.7 \pm 0.5$  K. This compound represents a singular SMM MOF built-up of Co-dimers with an anisotropic exchange interaction.

**Keywords:** MOF; single molecule magnet; slow magnetic relaxation; 2D coordination polymer; anisotropic exchange; magnetic dimer; Co(II) dimer

## 1. Introduction

Metal-organic frameworks (MOFs) are being intensively investigated due to their potential application in areas such as gas storage (e.g., fuel gases like hydrogen [1] and methane), capture of gases (e.g., greenhouse gases) [2], molecular sensing [3], separation [4] and catalysis [5], among others. A huge assortment of MOF topologies and different architectures can be accomplished by chemical design. The common characteristic of these open frameworks is that they are constructed from the assembly of inorganic sub-units (a single metal center, a cluster, or a chain) and organic linkers of different type (carboxylates,

phosphonates, azolates, etc.). The high absorption properties of porous MOFs are widely known, but in addition, different functionalities (magnetic [6], electrical [7], or optical [8]) can be incorporated into MOFs by adequately choosing the functional nodes, the organic linkers and their interconnection, or by including functional molecules in the pores.

The study of 3D MOFs counts with an impressive number of publications. The enormous interest in these materials is based on their rigidity and high porosity, which derives in interesting properties and potential applications [9]. On the other hand, the large horizontal and ultra-thin dimensions give the 2D MOF materials very high values for specific surface, atomic surface ratio, and number of active places exposed to surface. These could enhance some capabilities as compared to other nanomaterials or their bulky counterparts and create the premises for developing a new class of materials [10].

Coordination networks with magnetic properties are of particular interest. Four major types of magnetic MOFs are being investigated [11]: (i) MOFs with magnetic cooperativity, (ii) spin-crossover MOFs, (iii) MOFs with magnetocaloric effect (where the nodes possess an isotropic spin), and (iv) MOFs with slow magnetic relaxation, where the nodes are either single-ion magnets (SIMs) or single-molecule magnets (SMMs), or which embed single-chain magnets (SCMs).

Molecular magnets are a class of materials presenting intriguing physics, like slow relaxation and quantum tunneling of the magnetization, with attractive potential applications, e.g., in high density information storage, spintronics, and quantum computing. The controlled organization of nanomagnets into wider molecular edifices offers new exciting possibilities of architectures. On one hand, SMM-MOFs represent ideal models to investigate magneto-structural properties, such as the occurrence of relaxation behavior under different coupling schemes between the magnetic sub-units, or the competition with magnetic ordering, in different types of architectures. From a technological point of view, SMM-MOFs are interesting for quantum computing application, as the framework structure provides spatial separation between the qubit units, minimizing dipolar interactions, which produce the decrease of quantum coherence [11]. Furthermore, functional molecular species may be incorporated into the pores to tune the SMM properties or introduce a second property into the MOF. After the first SMM-MOFs prepared using  $Mn_4$  clusters [12], many other examples have been reported, based either on lanthanoids [13] or on transition metals [14].

Complexes with cobalt ions are particularly good candidates among the 3d transition metals for generating molecules that show slow relaxation of magnetization. Co(II) in an octahedral ligand field is especially interesting due to degenerate  $t_{2g}$  levels that are partially occupied, and thus orbital angular momentum is not totally quenched [15]. Early examples of Co(II) SMMs were based on tetranuclear cubanes [16]. Ever since, Co nanomagnets of various dimensionality, SIMs [17], SMM clusters [18], 1D [19], 2D [3] coordination polymers, as well as SCMs assembled in MOFs [20] and a few 3D networks [21] have been reported. Most of them require the application of an external field to show slow magnetic relaxations but there are also some examples of zero-field SMM behavior [16].

Examples of coordination polymers (CP's) containing  $Co_2$  dimers [15] with either antiferromagnetic (AF) [22] or ferromagnetic (FM) [23] intradimer coupling have been reported, though most works describe only the static magnetic characterization. However, SMM behavior has been demonstrated in a few 2D [24] and 3D [25] CPs built up from  $Co_2$  units.

The type and geometry of the chemical linkers between the sub-units play a crucial role in determining the architecture and thus the properties of the MOF. Among the numerous ligands, the most employed for the development of cobalt MOFs have been those having oxygen, water (hydroxide, alkoxide, alcohol, and carboxylate) or nitrogen (amine, pyridine, azide, and azole) coordinating atoms, and, in a few cases, sulfur (thiolate) [15]. The developments of metal-containing polymers have further expanded to include silicon: the so called organometallosiloxanes and polymeric derivatives (polyorganometallosiloxanes) containing Si-O-M bonds, or in which the metal is complexed through organic groups

attached to the siloxane moiety [26,27]. The metal can be inserted in the main chain or in side position [28]. In previous works, we have demonstrated the success of using highly flexible siloxane bridges in creating Co, Zn, and Mn-based 2D-MOFs [27,29,30].

In this work, we have prepared a new MOF that builds up from the staking of 2D CPs,  $\{[\text{CoCxAPy}] \cdot 2.15 \text{H}_2\text{O}\}_n$  (**1**), Cx = ditopic chelating organosiloxane ligand (1,3-bis(carboxypropyl)tetramethyldisiloxane dianion) and APy = 4,4'-azopyridine as co-ligands using similar procedure. The 2D-CP is built up by the interconnection of [CoCxAPy] 1D two-leg ladders with Co(II) dimer rungs. We report the magnetic properties of the compound **1**, showing that at low temperatures the dimer magnetism is dominant, where Co-Co rungs are weak AF coupled units exhibiting in-field SMM behavior. The single-ion properties were determined in a heteronuclear analogue,  $\{[\text{Zn}_{0.80}\text{Co}_{0.2}\text{CxAPy}] \cdot 1.5 \text{CH}_3\text{OH}\}_n$  (**2**), prepared by partial replacement of Co with non-magnetic Zn.

## 2. Results

### 2.1. Synthesis

Complex **1** was obtained by treating metal perchlorate ( $\text{Co}(\text{ClO}_4)_2$ ) with a mixture of ligands, 4,4'-azopyridine (APy), and 1,3-bis(carboxy)propyltetramethyldisiloxane ( $\text{H}_2\text{Cx}$ ), in a 2:1:1 molar ratio, in solution in the presence of 2,6-dimethylpyridine as a deprotonating agent. The first evidence of the complexation consists in the spectral changes of the compound (Figure S1a) with respect to the starting compounds: the disappearance of the absorption band characteristic of the carboxyl group from  $1715 \text{ cm}^{-1}$  and the appearance of the pairs of bands from 1601, 1447, and 1555,  $1385 \text{ cm}^{-1}$  assigned to  $\nu_{\text{as}}(\text{COO}^-)$  and  $\nu_{\text{s}}(\text{COO}^-)$  vibration bands in carboxylate having both bidentate chelating and bidentate bridging coordination modes [31]. The absorption band corresponding to the -N = N- bond appears at  $1425 \text{ cm}^{-1}$ , displaced from  $1410 \text{ cm}^{-1}$  in the free 4,4'-azopyridine. The presence of tetramethyldisiloxane fragments is mainly evidenced by the bands from  $1047 \text{ cm}^{-1}$  (Si-O-Si), 1254, and  $839 \text{ cm}^{-1}$  (Si-CH<sub>3</sub>).

The Co-Zn complex **2** has been prepared by the same procedure as complex **1**, by replacing the Co(II) salt with a mixture Co/Zn salts in a molar ratio of 5:95. The IR spectrum (Figure S1b) revealed the characteristic stretches assigned to carboxylate groups ( $\nu_{\text{as}}$  and  $\nu_{\text{s}}$ ) at about the same wavenumbers as in complex **1**, their magnitude of separation ( $\nu_{\text{as}} - \nu_{\text{s}}$ ) corresponding to the same coordination mode. The -N = N- stretching vibration is redshifted by  $13 \text{ cm}^{-1}$  compared to 4,4'-azopyridine, while the Si-O-Si and Si-CH<sub>3</sub> vibrations are found in the same position as in complex **1**, proving their structural similarity.

The values of the elemental analysis fit well with those calculated for the compound **1**. Slight deviation of the carbon content from the theoretical one in compound **2** could be attributed to some variations in the nature and weight of the crystallization solvents, compared to those found by crystallographic analysis (methanol in this case) as a result of exchange with the environment during the sample manipulation and storage in lab conditions. Calculations based on experimental values would indicate the replacement of most of the crystallization methanol with water, according to formulae  $\{[\text{Zn}_{0.80}\text{Co}_{0.2}\text{CxAPy}] \cdot 0.5\text{CH}_3\text{OH} \cdot 1.4\text{H}_2\text{O}\}_n$ . This is also supported by the results of the thermogravimetric analysis (Figure S2, Table S1), which show that in the first two stages, the compound **1** loses 5.5 wt% up to  $197.9 \text{ }^\circ\text{C}$  corresponding to cca.  $1.6 \text{ H}_2\text{O}$ , while the compound **2** loses 8.03 wt% up to  $159.6 \text{ }^\circ\text{C}$  corresponding to  $0.5 \text{ CH}_3\text{OH}$  and  $1.4 \text{ H}_2\text{O}$ . The  $T_{\text{peak}}$  values for the main mass losses are  $237.5$  and  $204.2 \text{ }^\circ\text{C}$  for the compounds **1** and **2**, respectively. Co:Zn molar ratio values estimated by EDX (Figure S3) and EDXRF (Figure S4) are close to each other and to that estimated by crystallographic analysis.

The DSC trace for the compound **1** (Figure S5) reveals the occurrence of a glass transition ( $T_g$ ), around  $17 \text{ }^\circ\text{C}$ . This is attributed to the tetramethyldisiloxane spacer in Cx ligand, which is very flexible and unable to develop significant intermolecular interactions, constituting the amorphous part of the structure. This may be a cause for which the diffractogram recorded at room temperature (Figure S6a) is slightly different from that simulated after single crystal X-ray diffraction experiments at  $200 \text{ K}$ . At room temperature,

which is above  $T_g$ , the flexible segments begins to relax, causing the interplanary distance to increase [32,33]. Another cause of the non-conformity of the experimental diffractograms with the theoretical ones found in the case of both compounds (Figure S6a,b) could be the adoption by the tetramethyldisiloxane segment of different conformations during the crystallization process that leads to various polymorph modifications. At the same time, the flexibility of the spacer doesn't affect the chemical model that was used to address the magnetic properties, since the chemical bonds, the coordination function of the ligands, and the coordination environment of the metal atoms do not differ.

## 2.2. Structural Characterization

The results of the X-ray diffraction study for **1** and **2** are summarized in Table 1. The structure of  $\{[\text{CoCxAPy}]\cdot 2.15 \text{H}_2\text{O}\}_n$  (**1**) is depicted in Figure 1. It is closely related to previously reported complex  $\{[\text{ZnCxApy}]\cdot 2\text{CH}_3\text{OH}\cdot 0.125 \text{H}_2\text{O}\}_n$  [29]. These compounds crystallize in the same space group P-1 of triclinic system with very similar unit cell parameters and differ only by co-crystallized solvate molecules. Both complexes contain the same formula unit in the asymmetric part of the unit cell.

**Table 1.** Crystallographic Data.

	1	2
CCDC	2005545	2005606
Empirical formula	$\text{C}_{22}\text{H}_{36.3}\text{CoN}_4\text{O}_{7.15}\text{Si}_2$	$\text{C}_{23.5}\text{H}_{38}\text{Co}_{0.2}\text{N}_4\text{O}_{6.5}\text{Si}_2\text{Zn}_{0.80}$
Formula weight	586.36	600.81
Temperature/K	200	200
Crystal system	triclinic	triclinic
Space group	P-1	P-1
$a/\text{\AA}$	11.8234(13)	11.7865(9)
$b/\text{\AA}$	11.8324(13)	11.8192(4)
$c/\text{\AA}$	13.3262(11)	13.3333(5)
$\alpha/^\circ$	110.597(8)	110.367(4)
$\beta/^\circ$	96.107(8)	96.376(5)
$\gamma/^\circ$	114.090(10)	114.261(5)
$V/\text{\AA}^3$	1523.5	1515.77(15)
Z	2	2
$D_{\text{calc}}/\text{mg}/\text{mm}^3$	1.278	1.316
$\mu/\text{mm}^{-1}$	0.685	0.882
Crystal size/ $\text{mm}^3$	$0.15 \times 0.10 \times 0.10$	$0.30 \times 0.10 \times 0.05$
$\theta_{\text{min}}, \theta_{\text{max}}(^\circ)$	4.938 to 50.048	3.97 to 50.052
Reflections collected	10714	11780
Independent reflections	5309	5329
	$[R_{\text{int}} = 0.0576]$	$[R_{\text{int}} = 0.0300]$
Data/restraints/parameters	5309/0/339	5329/0/350
$R_1^a (I > 2\sigma(I))$	0.0829	0.0438
$wR_2^b$ (all data)	0.2221	0.1198
GOF <sup>c</sup>	1.022	1.058
Largest diff. peak/hole/ $e \text{\AA}^{-3}$	1.21/−0.56	1.01/−0.30

<sup>a</sup>  $R_1 = \sum ||F_o| - |F_c|| / \sum |F_o|$ . <sup>b</sup>  $wR_2 = \{\sum [w(F_o^2 - F_c^2)^2] / \sum [w(F_o^2)^2]\}^{1/2}$ . <sup>c</sup> GOF =  $\{\sum [w(F_o^2 - F_c^2)^2] / (n - p)\}^{1/2}$ , where  $F_o$  and  $F_c$  are the observed and calculated structural factors, respectively,  $n$  is the number of reflections and  $p$  is the total number of parameters refined.

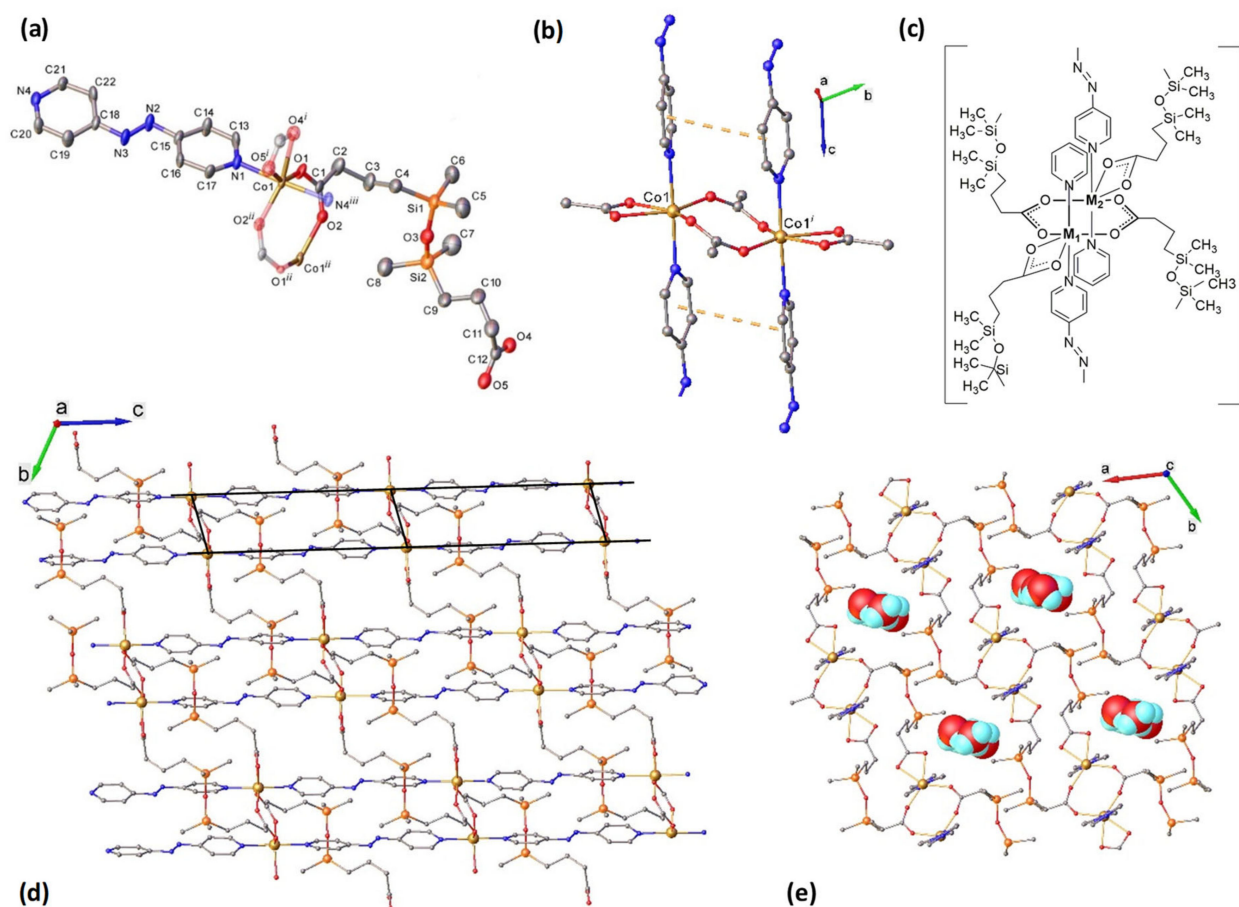


**Figure 1.** Structure of compound  $\{[\text{CoCxAPy}]\cdot 2.15 \text{H}_2\text{O}\}_n$  (**1**). (a) View of the asymmetric unit with atom labelling and thermal ellipsoids at 50% level. H atoms are omitted for clarity. Atoms obtained by symmetry-transformations are displayed semi-transparent. Symmetry codes:  $^i) x, y - 1, z - 1$ ;  $^j) 1 - x, 1 - y, 1 - z$ ;  $^k) x, y, 1 + z$ . (b) Co-Co dimeric unit conforming the ladder rungs. Centroid-to-centroid distance is of 4.0755(7) Å and slippage of 1.384 Å. (c) Line-drawing for dinuclear fragment: M1 = M2 = Co (**1**); M1 = Co; M2 = Zn (**2**); (d) Schematic representation of 2D-CP, formed by interconnection of the ladder-like structures running along the *c*-axis; (e) *ab*-plane view of the structure showing the pores where other molecules can be housed (e.g., water molecules in the figure).

The asymmetric unit of **1** shows that each Co(II) atom is six-coordinated in a  $\text{N}_2\text{O}_4$  strongly distorted octahedral geometry provided by four oxygen atoms from two  $\mu_2$ - $\kappa^2\text{O}:\text{O}'$  bridging and one  $\kappa^2\text{O}:\text{O}'$  chelating carboxylate groups in equatorial plane and two nitrogen atoms from APy ligands in apical positions (Figure 1a). The octahedral distortion parameter calculated as the sum of the deviation from  $90^\circ$  for all 12 *cis* bond angles is of  $74.82^\circ$  (Table S2).

In a centrosymmetric dinuclear unit two Co(II) ions are bridged at  $\text{Co}1 \cdots \text{Co}1(1 - x, 1 - y, 1 - z)$  distance of 4.042(2) Å through two  $\mu_2$ - $\kappa^2\text{O}:\text{O}'$  carboxylate bridging ligands (Figure 1b,c). These dinuclear fragments are interconnected via four rigid 4,4'-azopyridine (APy) conforming a two-leg ladder structure running along the *c*-direction. The separation between Co ions within the ladder rails is 13.331(7) Å.

A 2D coordination framework within the *bc*-plane is formed by the connection of Co dimers of adjacent ladders through four flexible 1,3-bis(3-carboxypropyl)tetramethyldisiloxane linkers (Cx) in *trans*-oide conformation (Figure 1d). The  $\text{Co} \cdots \text{Co}$  inter-ladder distance is 14.380(4) Å. The presence of offset face to face packing of adjacent APy ligands, which provide additional  $\pi$ - $\pi$  stacking interactions, strengthens the 2D network. This interaction seems to be strong enough to determine the non-planarity of the fragment comprising two cobalt atoms, two chelating, and two bidentate-bridging carboxylate ligands (Figure 1d).

The crystal structure is constructed from the parallel packing of the discrete, weakly interacting 2D layers. The methyl groups located on both sides of the 2D plane act as a hydrophobic screen that prevents the development of strong 3D intermolecular interactions (Figure 1c). All the interlayer distances are equal or exceed the sum of the Van der Waals radii for the corresponding atoms. This packing displays infinite channels along the *c*-axis accommodating fractally disordered solvate molecules (Figure 1e). Further analysis of intermolecular interactions has revealed the lack of interlayer H-bonding involving co-crystallized water molecules. These structural features indicate that compound **1** is porous. The solvent accessible void fraction calculated, for empty channels, by the Olex2 routine (for probe radii of 1.2 Å and 0.2 Å) constitute 0.21 related to unit cell volume.

According to X-ray crystallography, the heterometallic complex  $\{[Zn_{0.80}Co_{0.20}CxAPy] \cdot 1.5CH_3OH\}_n$  (**2**) (Table 1 and Table S3, Figures S7 and S8) is isostructural to **1**. Two metal ions in the dinuclear unit of **2** are joined via two  $\mu_2\text{-}\kappa^2\text{O}:\text{O}'$  carboxylate bridging ligands at 3.9684(8) Å distances. The separation of metal ions across Cx and APy linkers is of 11.1000(9) Å and 13.3333(5) Å, respectively.

### 2.3. Theoretical Model and Ab Initio Calculations

The ground state of the free Co(II) ion is  $^4F$  ( $L = 3$ ,  $S = 3/2$ ). In the crystal, Co(II) ions are six-coordinated in a strongly distorted octahedral geometry,  $C_{2v}$  point group. Under the octahedral ligand field the single-ion ground state is the  $^4\Gamma_4(^4T_1)$ , which is split into three orbital singlets by the orthorhombic field terms, each with fourfold spin degeneracy. Finally, the spin-orbit coupling splits the multiplet into six Kramer's doublets (KD's) [34].

In most cases, only the ground doublet and the next excited doublet at an energy  $\Delta$  are involved in the magnetic properties below room temperature. The spin-Hamiltonian formalism has been frequently used in the literature to describe the Zero Field Splitting (ZFS) of Co(II) complexes [35]. We have found this formalism adequate to describe magnetic properties of our complex below room temperature. The Hamiltonian describing single-ion properties in the presence of a magnetic field is given by:

$$\mathcal{H}_{SI} = D \left\{ \left[ S_z^2 - \frac{1}{3} S(S+1) \right] + \eta \left[ S_x^2 - S_y^2 \right] \right\} - \mu_B \vec{H} \hat{g} \vec{S} \quad (1)$$

The first two terms describe the orthorhombic Co(II) single ion anisotropy, where  $D$  and  $\eta = E/D$ , and the last term is the Zeeman term, with  $g$  the gyromagnetic factor for  $S = 3/2$  spin. At low temperatures magnetic interactions may be of relevance to describing the magnetic properties, and an exchange interaction term needs to be added to the Hamiltonian. In the present case of a Co(II)-Co(II) dimer with Co(II) in high spin state, one deals with the case of ions showing unquenched orbital angular momentum. For this reason, the conventional Heisenberg-Dirac-Van Vleck (HDVV) model is not applicable. In an excellent review [36] it is shown that the exchange interaction is orbitally dependent, and the main effect of the non-quenched orbital moment on the dimer Hamiltonian may be expressed, whichever the different approximations are applied, in terms of a phenomenological or a microscopic pseudospin  $S^* = 1/2$  Hamiltonian, when the Hamiltonian is projected onto the subspace of low-lying Kramer's doublets. Thus, we have proposed to use such a Hamiltonian in the present paper.

In  $\{[CoCxAPy] \cdot 2.15H_2O\}_n$  the Co-Co dimer building block has a center of symmetry, which prohibits the antisymmetric interaction, on one hand, and  $Co^{2+}$  is highly anisotropic, on the other. Therefore, a dimer Hamiltonian with orthorhombic anisotropy, described by an axial anisotropy  $D$  and an orthorhombic component  $E$ , and Zeeman term has allowed us to describe magnetic properties of this compound for the range of temperatures up to 300 K:

$$\mathcal{H}_{dim} = \sum_{i=1}^2 [D S_{i,z}^2 + E (S_{i,x}^2 - S_{i,y}^2)] - 2J (\vec{S}_1 \cdot \vec{S}_2) - \mu_B \sum_{i=1}^2 \vec{H} \hat{g} \vec{S}_i \quad (2)$$

operating on the dimeric  $S = 3/2 \otimes S = 3/2$ , 16-fold wave function base. The influence of orbital momentum is implicit in the principal values of local zero-field splitting tensor, on the one hand, and the local  $g$ -tensors, on the other hand.

Following Palić's receipt [36], at low temperature, the dimer anisotropic Hamiltonian acting on the  $S^* = 1/2 \otimes S^* = 1/2$  four-fold dimer wave functions  $\{ \frac{1}{2} |1/2, \pm 1/2\rangle |1/2, \pm 1/2\rangle \}$  is:

$$\mathcal{H}_{dim}^* = -2 \left( J_x^* S_x^{*1} S_x^{*2} + J_y^* S_y^{*1} S_y^{*2} + J_z^* S_z^{*1} S_z^{*2} \right) + \mu_B \sum_{i=1}^2 \left( g_x^* S_x^{*i} H_x + g_y^* S_y^{*i} H_y + g_z^* S_z^{*i} H_z \right) \quad (3)$$

where  $J^*_\alpha \ll D$ ,  $\alpha = x, y, z$  are the main axes of the  $g^*$  and the  $J^*$  tensors, which are coincident.

In order to determine single-ion energy levels and identify an appropriate magnetic model, relativistic *ab initio* calculations have been performed, using the CASSCF/NEVPT2 method [37,38], as implemented in the ORCA 4.0 program [39,40]. In this method, the spin-orbit coupling and the spin-spin coupling relativistic effects, which are at the origin of the magnetic anisotropy, are included *a posteriori*. The *ab initio* calculations were done on a simplified version of the Co<sub>2</sub> dimer fragment of compound **1** and **2**, where the Cx ligands were replaced by propionate and the APy ligands by pyridine (see Figure 2b) and where atomic positions were obtained from the experimental structure. In addition, one of the Co(II) ions was replaced by a diamagnetic Zn(II) ion. The basis-set was the DKH-Def2-TZVP [41] for all the atoms, which incorporates scalar relativistic effects. To speed up the calculations, the SARC/J auxiliary basis [41] along with the resolution of identity (RI) [42] and the chain-of-spheres (COSX) approximations [43] were used. In the CASSCF calculations, the active space was considered to be 10 Co(II) 3d and 3d' orbitals containing 7 electrons (CASSCF(7,10)). Ten quartets and eleven doublets were used for the state-averaged CASSCF calculation. Then, the NEVPT2 calculations were performed with the CASSCF(7,10) reference space for the treatment of the dynamical correlation energy. After that, the effect of the spin-orbit coupling was taken into account using a mean-field operator (SOMF) [44,45], which was diagonalized on the basis of the previous CASSCF wavefunctions. After diagonalization of the *ab initio*  $g^*$ -tensor for **1**, the eigenvalues were:  $g_1^* = 6.05$ ,  $g_2^* = 3.82$  and  $g_3^* = 1.91$  (Table 2). The calculated Easy Axis of Magnetization (EAM) is depicted in Figure 2b. The hard axis is directed along the N-Co-N ligands axis, whereas the easy axis lies in the equatorial plane, near perpendicular to the Co-Co rung. The calculated ligand field is highly orthorhombic, with parameters  $\eta = E/D = 0.13$ , and  $D/k_B = 82$  K. The calculated energy levels of the six KD's are shown in Figure 2c. The energy gap between the ground KD and the first excited one is  $\Delta/k_B = 166$  K. Very similar parameters are obtained from *ab initio* calculations of the diluted complex, **2** (Table 2).

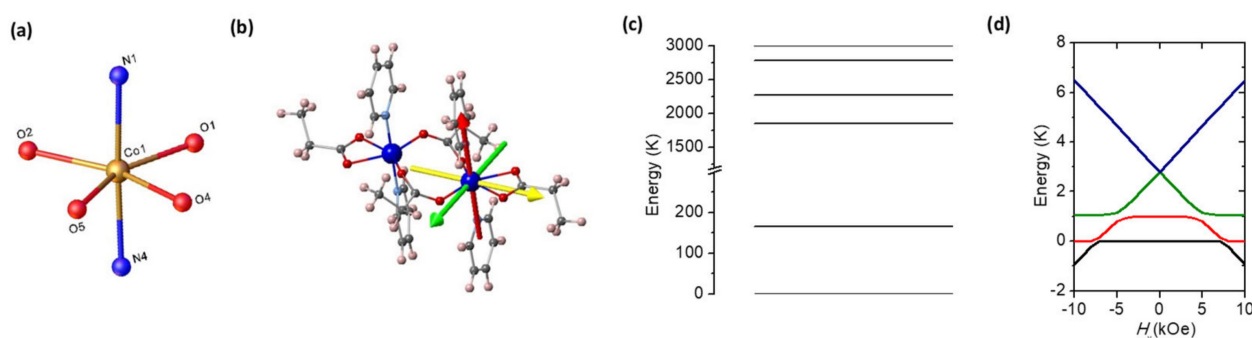


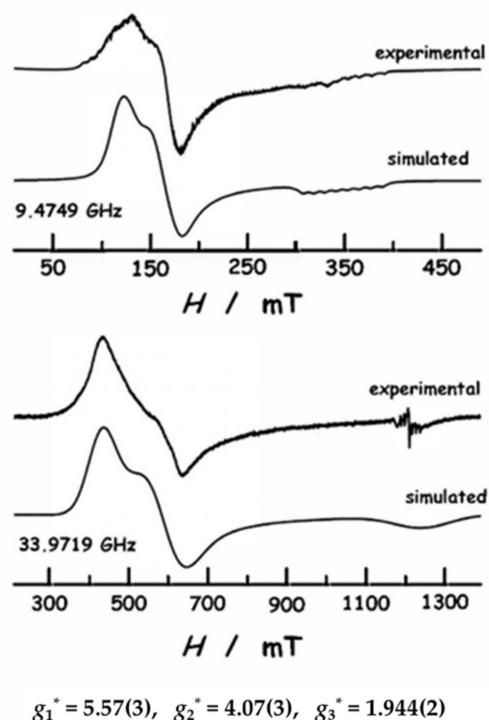
**Figure 2.** Single-ion properties. (a) Coordination sphere around Co(II) ion; (b) *ab initio* calculated easy axes of magnetization (the hard axis (HA, in red) is along the N-Co(II)-N axis; the easy axis (EA, in green) and intermediate axis (IA, in yellow) lie in the equatorial plane); (c) *ab initio* calculated energy levels of the six Kramer's doublets; (d) energy level diagram for Co(II)-Co(II)  $S^* = 1/2$  dimer, with  $J^*_x/k_B = -0.5$  K,  $J^*_y/k_B = -2.3$  K and  $J^*_z/k_B = -0.5$  K, as a function of magnetic field applied along easy axis.

**Table 2.** Summary of parameters of single-ion ZFS Hamiltonian given by Equation (1). *ab initio* and experimental, together with  $S^* = \frac{1}{2}$  ground state KD1  $g^*$ -factors.

		<i>Ab initio/Fit</i> Compound 1	<i>Ab initio</i> Compound 2	<i>Experimental</i>
$S = 3/2$	$D/k_B(K)$	82.0	83.0	
	$\eta = E/D$	0.13	0.20	0.165(5)
	$J/k_B(K)$	−0.32		−0.44
	$g_x$	2.40	2.37	2.74(3)
	$g_y$	2.58	2.64	2.28(2)
	$g_z$	1.96	1.95	2.11(1)
$S^* = 1/2$	$g_x^*$	3.82	3.28	4.07(3)
	$g_y^*$	6.05	6.58	5.57(3)
	$g_z^*$	1.91	1.79	1.944(2)

#### 2.4. EPR Spectroscopy

EPR measurements on a polycrystalline sample of diluted compound 2 were performed to determine experimentally the anisotropic  $g^*$  tensor principal values. Pure complex 1 is EPR silent, which may be indicative of a singlet ground state due to intradimer interactions; this will be shown below. Figure 3 displays the X-band and Q-band spectra measured at  $T = 6$  K. Both spectra exhibit two features corresponding with the highest principal values of the  $g^*$  tensor ( $g_1^* \approx 5.6$ ,  $g_2^* \approx 4.1$ ). On the other hand, the high field feature ( $g_3^* \approx 1.9$ ) is hardly observed in the Q-band spectrum, and overlaps with a signal that is due to the quartz tube sample-holder, separately measured. The simulated spectra, calculated with the help of EasySpin [46] using these principal values, are in good agreement with the experimental spectra.

**Figure 3.** X-band (9.475 GHz, top) and Q-band (33.972 GHz, bottom) EPR spectra of the polycrystalline diluted sample 2 measured at  $T = 6$  K, plotted as a function of magnetic field. Comparison of spectra with the simulation, calculated with EasySpin using the  $g^*$  parameters given in the lower part of the graph and collected in Table 2.

As a summary, the dominant EPR signal can be described with an effective spin  $S_z^* = 1/2$  with a gyromagnetic tensor with the principal values  $g_1^* = 5.57 \pm 0.03$ ,  $g_2^* = 4.07 \pm 0.03$  and  $g_3^* = 1.944 \pm 0.002$ . The effective magnetic moment  $\mu = 3.58 \pm 0.08 \mu_B$  was calculated as  $\mu(\mu_B) = g_{av}^* \sqrt{S^*(S^* + 1)}$ , with the average gyromagnetic moment,  $g_{av}^* = ((g_1^{*2} + g_2^{*2} + g_3^{*2})/3)^{1/2} = 4.138$ . The predicted low temperature Curie factor is  $C_{EPR} = 1.61 \pm 0.01 \text{ emu}\cdot\text{K/mol}$ .

As previously introduced, the single-ion ground state of Co(II) in a distorted octahedral ligand field preserves an important orbital contribution. Despite of this, we have made use of spin Hamiltonian formalism to describe magnetic properties up to room temperature. More elaborated models, which explicitly include spin orbit coupling, have been used in the literature to account for the effects of high energy levels [47]. However, such models have some limitations in the interdependency of the parameters and the unicity in fitting the magnetometry experimental results. Therefore, we deem appropriate the use of ZFS formalism in the present study.

Hence, the description of the two lowest Kramer's doublets (KD1 and KD2) is given in terms of an effective spin  $S = 3/2$  including a zero field term as described by Equation (1).

From the EPR point of view, given that the separation in energy of the two doublets  $\Delta/k_B = 2D/k_B(1 + 3\eta^2)^{1/2}$  is much larger than the microwave energy, the system can be described by two  $S^* = 1/2$  systems with different effective  $g^*$  tensors [48]. As it was obtained by *ab initio*,  $D > 0$ , therefore the ground KD1 corresponds to the  $M_S = \pm 1/2$  components of the  $S = 3/2$  and the principal values of the  $g^*$  tensor are given by Pilbrow's equations [49]:

$$\begin{aligned} g_x^* &= g_X \left( 1 + \frac{1-3\eta}{\sqrt{1+3\eta^2}} \right) \\ g_y^* &= g_Y \left( 1 + \frac{1+3\eta}{\sqrt{1+3\eta^2}} \right) \\ g_z^* &= g_Z \left( \frac{2}{\sqrt{1+3\eta^2}} - 1 \right) \end{aligned} \quad (4)$$

which relate the apparent  $g_{x,y,z}^*$  values within the ground state KD and the true  $g_{x,y,z}$  values of  $S = 3/2$  as given in Equation (1) Hamiltonian. According to Equation (4), we may assign the EPR obtained gyromagnetic values,  $g_1^*$ ,  $g_2^*$ , and  $g_3^*$ , to the corresponding  $g_x^*$ ,  $g_y^*$ , and  $g_z^*$  in the single-ion main axis system as  $g_x^* = g_2^* = 4.07 \pm 0.03$ ,  $g_y^* = g_1^* = 5.57 \pm 0.03$  and  $g_z^* = g_3^* = 1.944 \pm 0.002$ .

Therefore, the positive  $D$  value is stabilizing in energy the lowest  $M_S$  doublet of the  $S = 3/2$  multiplet. This implies that we have an easy plane anisotropy, consistent with *ab initio* calculations, where the axial z-axis is the hard magnetic axis, and the easy axis lies in the equatorial plane, along the y-axis.

## 2.5. Static Magnetic Properties (Up to Room T)

Figure 4 plots the temperature dependence of  $\chi \cdot T$  for pure compound **1** and diluted complex **2**. Shown data have been corrected from a temperature independent susceptibility term,  $\chi$ , ( $\chi_0 = -7.0 \times 10^{-4} \text{ emu/mol}$  for **1** and  $\chi_0 = -1.7 \times 10^{-3} \text{ emu/mol}$  for **2**). This term accounts for the Van Vleck contribution of Co(II) high energy levels, and the dominant diamagnetic contribution of the Daphne Oil used to fix the sample grains ( $\chi_{dia}$  between  $-1 \times 10^{-3}$  and  $-2 \times 10^{-3} \text{ emu/mol}$ ). Both compounds show saturation to about  $2.7 \text{ emu}\cdot\text{K/mol}$  at 300 K. This value is significantly higher than the theoretical spin-only value  $\chi \cdot T = 1.88 \text{ emu}\cdot\text{K/mol}$  predicted for an  $S = 3/2$  ( $g = 2.00$ ), indicating a relevant orbital contribution, as commonly observed for Co(II) compounds. As the temperature is lowered,  $\chi \cdot T$  continuously decreases due to the depopulation of electronic states.  $\chi \cdot T$  decreases faster below 100 K, reaching a value of  $1.6 \text{ emu}\cdot\text{K/mol}$  at 2 K in the diluted compound, indicative of significant ZFS. This value is in perfect agreement with previously found low temperature Curie factor  $C_{EPR} = 1.61 \pm 0.01 \text{ emu}\cdot\text{K/mol}$ . In the pure compound,  $\chi \cdot T$  tends to zero at very low temperatures, indicating the presence of antiferromagnetic interactions between the Co ions.

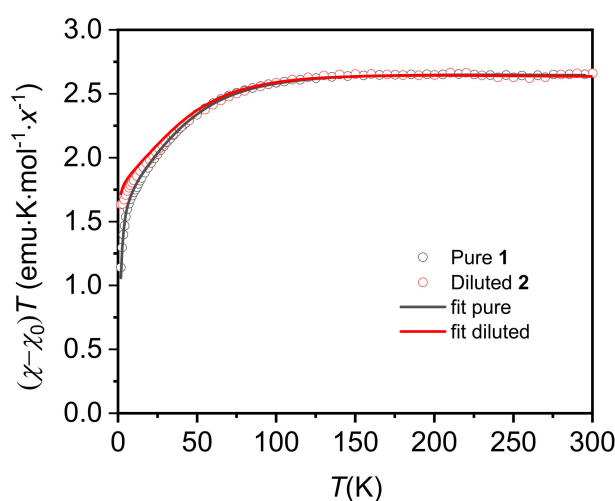


**Figure 4.** Temperature dependence of  $(\chi - \chi_0)T$  for pure **1** ( $x = 1$ ) and diluted compound **2** ( $x = 0.2$ ), measured at  $H = 1$  kOe. In line are shown the simulated curves as obtained from Equation (2) with the  $D$ ,  $E$ , and  $g$ 's from the *ab initio* calculations of **1** and **2** and using  $J$  as a fitting parameter  $J/k_B = -0.32$  K for **1**. Experimental data were corrected from a temperature independent term,  $\chi_0 = -7.0 \times 10^{-4}$  emu/mol for **1** and  $\chi_0 = -1.7 \times 10^{-3}$  for **2**.

The temperature dependence of the magnetic susceptibility can be modeled with *ab initio* obtained energy levels and adjusted to parameters described by the spin Hamiltonian of Equation (2). Results are depicted in Figure 4 and compared with  $\chi \cdot T$  temperature dependence of pure **1** and diluted compound **2**.

Complementary, the magnetic susceptibility in the high temperature range,  $T > 150$  K, has been analyzed in the frame of a Curie-Weiss law approximation

$$\chi(T) = \chi_0 + \frac{C}{(T - \theta)} \quad (5)$$

where  $C$  is the Curie constant,  $\chi_0$  is the temperature independent contribution to the magnetic susceptibility and Curie temperature,  $\theta$ , accounts for the magnetic interactions with the neighboring atoms. By fitting Equation (5) to the experimental data in the high temperature range (see Figure S9) the values shown in Table 3 were found. The obtained Curie constant,  $C = 2.67$  emu·K/mol, corresponds to an effective magnetic moment  $\mu_{\text{eff}} = 4.62 \mu_B$ , much larger than the spin-only contribution,  $\mu_S = 3.87 \mu_B$  ( $S = 3/2$ ,  $g = 2.00$ ), indicating an important orbital coupling. From this effective moment we deduce an average value for the gyromagnetic factor for the  $S = 3/2$  four levels system,  $g_{\text{eff}} = 2.39$ .

**Table 3.** Fit parameters of  $\chi^{-1}(T)$  data to a Curie-Weiss law.

	Pure <b>1</b>	Diluted <b>2</b>
$\chi_0$ (emu·mol <sup>-1</sup> )	$-7.0 \cdot 10^{-4}$	$-1.7 \cdot 10^{-3}$
$C$ (emu·K/mol)	$2.672 \pm 0.008$	$2.67 \pm 0.01$
$\theta$ (K)	$-1.1 \pm 0.7$	$-0.1 \pm 0.3$

Considering  $g_{\text{eff}}^2 = (g_x^2 + g_y^2 + g_z^2)/3$ , together with the relations given in Equation (4), yields a value for the orthorhombic factor of  $\eta = E/D = 0.165$ . Furthermore, we can determine the main values of the  $g$ -tensor for the  $S = 3/2$ ,  $g_x = 2.74$ ,  $g_y = 2.28$ , and  $g_z = 2.11$ . These values largely deviate from the spin-only isotropic  $g = 2.00$  confirming a significant spin-orbit contribution. Notably, the  $\eta = E/D$  factor is very similar to the value determined by *ab initio* calculations (see Table 2).

The Curie temperature  $\theta = -1.1$  K gives information of the sign and magnitude of the interaction in the dimer. Within the mean field theory,  $\theta = 2zJS(S + 1)/3k_B$ , where  $z$  is the

nearest neighbors number and  $J$  is the average interaction. For a  $S = 3/2$  dimer,  $z = 1$ , with exchange interaction  $H = -2JS$ , we obtain an average AF interaction in the Co(II) dimer of  $J/k_B = -0.44$  K, close to the exchange interaction used to fit  $\chi \cdot T$  curve of **1** with *ab initio* parameters,  $J/k_B = -0.32$  K.

## 2.6. Static Magnetic Properties ( $T < 20$ K)

The field dependence of the magnetization of a powdered sample measured at  $T = 2.0$  K up to 140 kOe is shown in Figure 5a for pure **1** and diluted **2** compounds. The magnetization per Co ion is represented as a function of reduced  $\mu_0 H/k_B T$ . The  $M(H)$  dependence for a powder, spatially averaged moment, has been calculated, according with Equation (3), with the  $g^*$  tensor parameters obtained by EPR ( $g_x^* = 4.07$ ,  $g_y^* = 5.57$ ,  $g_z^* = 1.944$ ). A Van Vleck contribution,  $\chi_{\text{TV}} = 1.8(1) \cdot 10^{-2} \text{ emu} \cdot \text{mol}^{-1}$ , was added to fit the experimental  $M(H)$  data. The simulated curve fits perfectly the experimental data for the diluted compound **2**, where the exchange interaction is negligible. The agreement is satisfactory and proves the adequacy of using the  $S^* = 1/2$  approximation at low temperatures, on one hand, and that the Co(II) ground state has an orthorhombic anisotropy, on the other hand. The  $M(H)$  curve for pure **1** lies below that of the diluted compound **2**, which can be attributed to an AF interaction within the Co(II) dimer. Indeed, a good fit of the  $M(H)$  for the pure compound was achieved with the above  $g^*$  single-ion tensor components, and the dimeric anisotropic exchange components  $J_x^*/k_B = -0.5$  K,  $J_y^*/k_B = -2.3$  K, and  $J_z^*/k_B = -0.5$  K, which are the best-fit parameters of low temperature  $\chi(T)$ ,  $M(H)$ , and heat capacity analysis (*vide infra*).

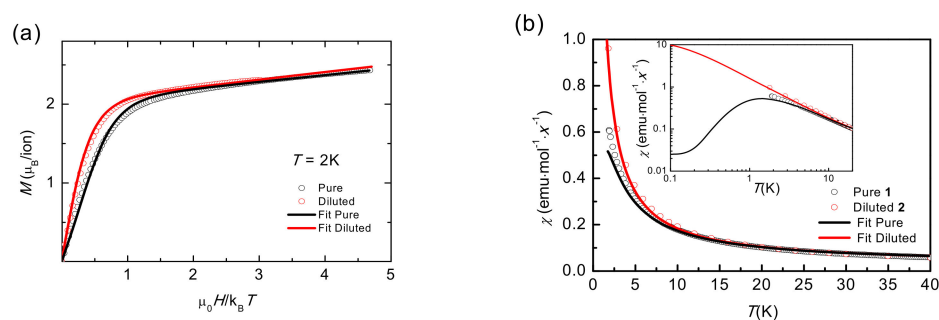


**Figure 5.** (a) Field dependence of the magnetization,  $M(H)$ , measured at  $T = 2$  K for **1** and **2**. (b) Low temperature detail of magnetic susceptibility  $\chi(T)$  data at 1. kOe for **1** ( $x = 1$ ) and **2** ( $x = 0.2$ ). The lines correspond to fits with Equation (3) using the  $g^*$  components deduced from the EPR measurements, the intra-rung anisotropic exchange constants  $J_x^*/k_B = -0.5$  K,  $J_y^*/k_B = -2.3$  K, and  $J_z^*/k_B = -0.5$  K, and integrating over the randomly oriented grains. A Van Vleck contribution is added to the magnetization simulated curves. For the diluted compound the dimer exchange interaction is not considered in the calculation.

The adequacy of the dimer model and its anisotropic character is further corroborated by the simulation of the low temperature magnetic susceptibility  $\chi(T)$ . Figure 4 shows the experimental data for pure **1** and diluted **2** compounds together with simulations. The dimer model perfectly fits the susceptibility for **1**. For AF coupling, the  $\chi(T)$  shows a maximum at a temperature of the order of the interaction, as shown in Figure 5b inset, not observed experimentally since it falls below the measured temperature range. Furthermore, when the interaction is canceled, as for the diluted compound **2** the curve is perfectly simulated with the Zeeman term as indicated in Equation (3).

## 2.7. Heat Capacity

The measurement of heat capacity is not commonly used in the study of magnetic molecules although it can be complementary and provide valuable information on electronic levels and the energy of phonons, as well as magnetic interactions [50]. In some cases the determination of the low temperature heat capacity has been key to determining the

slow relaxation mechanisms in SMM metal complexes [51]. In the present case, seeking to obtain more information of the magnetic interactions, the heat capacity (HC) of a powdered sample of compound **1** was measured as a function of the temperature, under different applied fields ranging from  $0 < H < 30$  kOe (Figure 6a). The lattice contribution,  $C_L/R = \alpha T^{-n}$ ,  $\alpha = 6.35 \times 10^{-3} \text{ K}^n$ ,  $n = 2.3$ , dominated at high temperatures ( $T > 10$  K), and was subtracted from the experimental data to obtain the magnetic contribution,  $C_m/R$ , which is shown in Figure 6b,c.

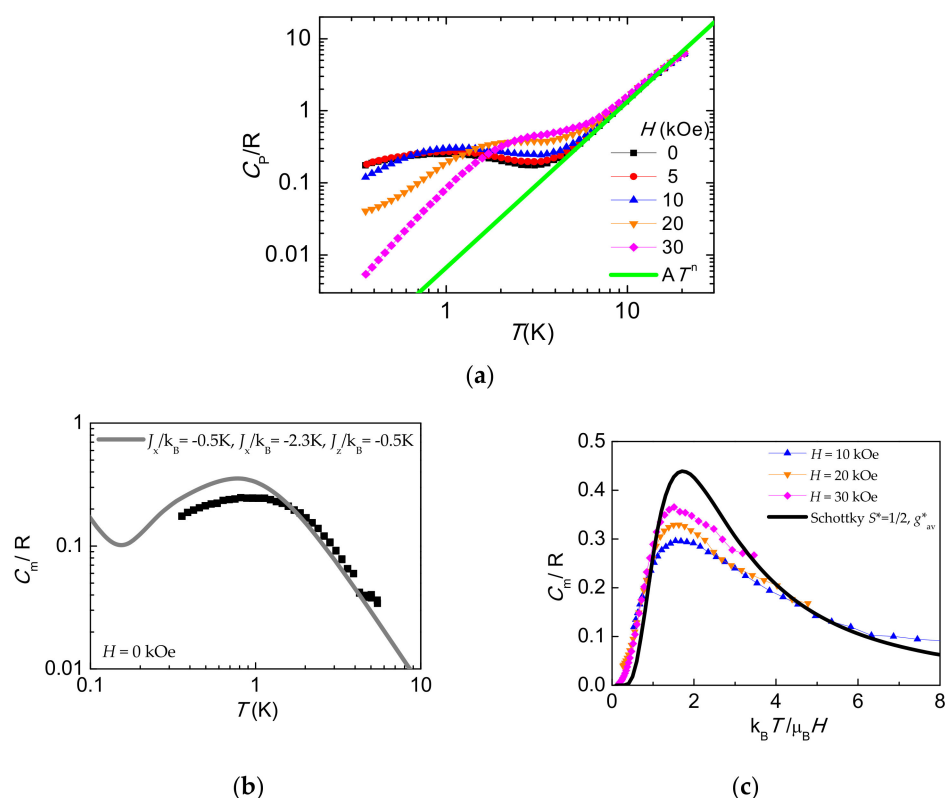


**Figure 6.** (a) Heat capacity as a function of temperature for various applied fields for compound **1**. The lattice contribution is depicted by the solid green line. (b) Magnetic contribution to the heat capacity as a function of temperature for  $H = 0$ . The solid grey line is the simulated  $C_m(T)$  curve as obtained within the dimer model given in Equation (3), with anisotropic AF exchange constants,  $J_x^*/k_B = -0.5 \pm 0.05 \text{ K}$ ,  $J_y^*/k_B = -2.3 \pm 0.3 \text{ K}$ , and  $J_z^*/k_B = -0.5 \pm 0.05 \text{ K}$  plus a hyperfine contribution. (c) Magnetic heat capacity contribution as a function of the adimensional  $x = k_B T / \mu_B H$ . Continuous black line: calculated two-level Schottky curve with  $g_{av}^* = 4.138$ .

The magnetic heat capacity at zero field displays a rounded contribution centered around 1 K which may be attributed to low dimensional or short range magnetic ordering. Although the curve is featureless, the broadness and extension indicates that it has to comprise different contributions, which cannot be accounted for with a simple model. In view of the structure of the compound, where the separation between the intra-rung Co-Co ions is much smaller than the inter-rung separation, a magnetic dimer model with anisotropic exchange interaction, as defined by Equation (3), was adopted to fit the magnetic contribution to the heat capacity. The best compromise in reproducing the  $C_m(T)$  at  $H = 0$  kOe curve (see Figure 6b), together with  $M(H)$  at 2 K and  $\chi(T)$  at low  $T$ , was obtained for the following set of exchange parameters,  $J_x^*/k_B = -0.5 \pm 0.05 \text{ K}$ ,  $J_y^*/k_B = -2.3 \pm 0.3 \text{ K}$ , and  $J_z^*/k_B = -0.5 \pm 0.05 \text{ K}$ , which are fully compatible with the orthorhombic character of the Co(II) ground state. Indeed, the anisotropic exchange interaction splits the four energy levels of the dimer ( $S_1 \otimes S_2 = 0, 1$ ) (see Figure 2d), giving as a result a broad contribution of the HC at zero magnetic field. The change in magnetic entropy below 10 K, reaching 0.5–0.6 R per Co ion supports this model (see Figure S10).

When a magnetic field is applied, the exchanged split levels of Co(II) dimer are further separated, and at high magnetic field the  $C_m(T, H)$  curves are dominated by the Zeeman term. They converge to a two-level Schottky anomaly with EPR  $g^*_{av} = ((g^*_x{}^2 + g^*_y{}^2 + g^*_z{}^2)/3)^{1/2} = 4.138$  as illustrated in Figure 6c where the  $C_m(T)$  at different fields are plotted as a function of the adimensional parameter  $k_B T / \mu_B H$ .

At very low temperatures the hyperfine contribution (hf) to the heat capacity has to be taken into account. The natural abundance of the  $I = 7/2$  isotope ( $^{59}\text{Co}$ ) is 100% and its nuclear moment is  $\mu = 4.613 \mu_N$ . The hyperfine heat capacity at high temperatures may be approximated to:

$$C_{hf}/R = \frac{A^2 I(I+1)}{12k_B^2} \frac{1}{T^2} = \frac{b}{T^2} \quad (6)$$

where  $A$  is the average hf interaction constant formulated for a  $S^* = \frac{1}{2}$ . A value of  $b = 1.66 \times 10^{-3} \text{ K}^2$  [52] has been considered in the simulation, similar to other values reported in the literature for Co organic complexes [53]. The hyperfine contribution is much smaller than the spin exchange interaction, introducing additional degrees of freedom and splitting the electronic levels at very low temperature.

### 2.8. Dynamic Magnetic Properties

Magnetic relaxation phenomena of compound **1** were explored by ac susceptibility measurements as a function of frequency, dc magnetic field strength, and temperature.

No out-of-phase signal ( $\chi'' = 0$ ) was observed in the measured frequency range, from 0.1 Hz to 10 kHz, at zero dc magnetic field indicating an isothermal response of the spin system through fast spin relaxation. However, when an external dc field was applied an increase of the  $\chi''$  signal was observed for fields larger than  $H = 1 \text{ kOe}$  (see Figure 7a,b). Two different field-induced slow relaxation of the magnetization processes were well distinguished, one at very low frequencies at the edge of the lower-frequency measurement window, and another process lying at the high-frequency edge. Given that it is a randomly oriented sample, it may be inferred that the anisotropic spin system participates in one or another mechanism depending on the relative orientation with respect to the external magnetic field. Other faster relaxation pathways are not excluded.

Since for most of the  $\chi''(f)$  curves no maximum was attained within experimental frequency range, the estimation of the relaxation times was obtained from the expression [50]:

$$\tau(T, H) = \frac{\chi''(f, T, H)}{(\chi'(f, T, H) - \chi_\infty(T, H)) \cdot 2\pi f} \quad (7)$$

where  $\chi_\infty$  is the adiabatic susceptibility at the limit of high frequency ( $f \rightarrow \infty$ ), when spins are not responding to magnetic field. For the low frequency process ( $f < 1 \text{ Hz}$ ), the adiabatic susceptibility can be easily determined by the value at 100 Hz,  $\chi_\infty^{\text{lf}} = \chi'(100 \text{ Hz})$ . Note that 100 Hz can be considered as high frequency in comparison to  $f < 1 \text{ Hz}$ . For the high frequency process the determination of the adiabatic susceptibility was more intricate (see SI.4 for details).

The obtained relaxation times for the two processes,  $\tau_{\text{lf}}$  and  $\tau_{\text{hf}}$ , as function of the magnetic field and the inverse of the temperature are depicted in Figure 7c,d, respectively. The low frequency relaxation time is nearly independent on the magnetic field and temperature,  $\tau_{\text{lf}} \approx 2 \text{ s}$ . It is a likely process only at the lowest temperatures and increasing in amplitude with field, i.e., the number of centers exhibiting slow relaxation and being blocked at high frequencies increases with increasing magnetic field. On the other hand, the high frequency relaxation process has a slight dependence with field, decreasing the relaxation time as field increases.

The fit of the high temperature range of  $\tau_{\text{hf}}(1/T)$  to an Arrhenius law,  $\tau = \tau_0 \exp(U/k_B T)$ , affords an effective energy barrier for the reversal of the magnetization of  $U/k_B = 6.7 \pm 0.5 \text{ K}$  and prefactor  $\tau_0 = 1.9 \pm 0.2 \times 10^{-6} \text{ s}$ . This energy is of the order of the energy separation between states within the magnetic dimer model (see Figure 2d). Thus, this process is ascribed

to an Orbach mechanism within the dimer levels. At low temperatures, the relaxation time evolves to a direct process mechanism. Attempts to reproduce the temperature dependence of the high frequency process assuming a direct process and a Raman mechanism were unsuccessful.

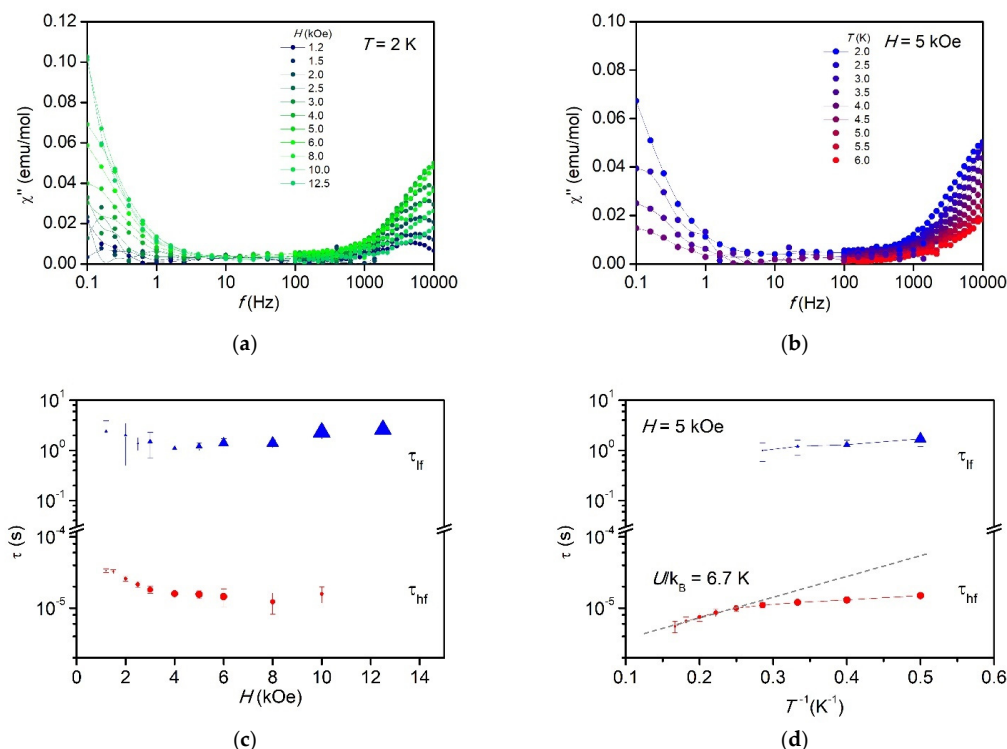


**Figure 7.** Magnetic relaxation for compound **1**. Top: Out-of-phase component of the susceptibility as function of frequency, (a) at constant  $T = 2$  K and diverse applied fields, and (b) at constant field  $H = 5$  kOe and different temperatures. Bottom: spin relaxation time as a function of the field,  $\tau(H)$  at  $T = 2$  K (c), and as a function of the inverse temperature,  $\tau(1/T)$  at  $H = 5$  kOe (d), for the two different observed processes,  $\tau_{lf}$  and  $\tau_{hf}$ .

The observation of a very slow process at low temperatures indicates a partial blockage of the magnetization in coexistence with a faster relaxation mechanism. The obtained relaxation times, although of the order of seconds, are not slow enough to observe the opening of the hysteresis loop at 1.8 K at the fastest speed achievable in our experimental system, 180 Oe/s.

### 3. Discussion

In compound **1**, the interaction path in the dimer rung is via two carboxylate bridges Co-O-C-O-Co. Most, if not all, of the reported exchange interactions in carboxylate bridged Co-Co complexes are antiferromagnetic [15]. However, its strength depends on the modes of connection (syn–syn, syn–anti, or anti–anti), the angles, and also on the Co-Co distance.

To check this in more detail, in Table 4 Co-Co dimers with carboxylate exchange paths bridging both metal atoms have been collected. Furthermore, those compounds with carboxylate and oxygen mediated bridges are included. As a third group, two cases with oxalate bridges have been also included for comparison's sake.

**Table 4.** Compounds with Co-Co exchange interaction (spatial interaction dimension). Reference. Co coordination. Exchange path: carboxylate paths (Co-O-C-O-Co) { in parenthesis (#) number of carboxylate paths, type of path}, and oxygen mediated path (Co-O-Co). Co-Co distance. C, Curie constant (for comparison purposes, the C value given in this Table assumes 2 Co per f.u; for a Co(II) dimer,  $C = 3.75 \text{ emu}\cdot\text{K/mol}$  for spin only  $3/2$ ),  $\theta$ , Curie–Weiss temperature,  $g$ , gyromagnetic factor ( $g^*$  in effective spin  $S = 1/2$  ground state), sub-indexes indicate directions ( $x, y, z$ ), or spin subsystems. Exchange interaction Hamiltonian, transformed to the  $H_H = -2JS_1S_2$  (Heisenberg),  $H_I = -2JS_{z1}S_{z2}$  (Ising) or  $H_{AN} = -2J(S_{z1}S_{z2} + e_xS_{x1}S_{x2} + e_yS_{y1}S_{y2})$  (Anisotropic) conventions, Spin,  $S = 3/2$  model, or effective spin  $S^* = 1/2$  model.  $J/k_B$ , exchange interaction constant.  $D/k_B$ , anisotropy constant.

	Ref.	Coord.	Exch. Path	Co-Co (Å)	C (emu·K/mol dimer)	$\theta$ (K)	$g$	Model Spin	$J/k_B$ (K)	$D/k_B$ (K)
<b>Co-Co Carboxylate Exchange Paths</b>										
$\text{Co}_2(\text{esp})_2(\text{EtOH})_2$ (dimer)	[55]	CoO4L L-outwards	(4) syn-syn	2.7245	~4.4		$g_{\perp} = 2.10$ $g_{\parallel} = 3.5$	$H_H$ 3/2	−9.49 AF	−79
$\{[\text{CoCxAPy}] \cdot 2.15 \text{H}_2\text{O}\}_n$ (2LL dimer)	This work.	CoN <sub>2</sub> O <sub>4</sub> apical	(2) syn-syn	3.9684	5.35	−1.1	$g_x = 2.40$ $g_y = 2.58$ $g_z = 1.96$	$H_H$ 3/2	−0.32	82 $\eta = 0.13$
“	“	“	“	“			$g_x^* = 4.07$ $g_y^* = 5.57$ $g_z^* = 1.94$	$H_{AN}$ 1/2	−2.3 $e_x = 0.2$ $e_y = 0.2$	
$[\text{Co}(\text{Htatb})(\text{bimbp})] \cdot \text{DMF}$ (dimer)	[54]	CoN <sub>2</sub> O <sub>4</sub> apical	(2) syn-syn	4.156	3.73	−7.21	2.28	$H_H$ 3/2	−6.65 AF	
$[\text{Co}(\text{Htatb})(1,3\text{-bimyb})]$ (dimer)	[54]	CoN <sub>2</sub> O <sub>4</sub> apical	(2) syn-syn	4.176	3.69	−8.44	2.4	$H_H$ 3/2	−5.23 AF	
$[\{\text{Co}(\text{phen})\}_2(\text{fum})_2]$ (dimer)	[58]	CoN <sub>2</sub> O <sub>4</sub> adjacent	(2) distorted syn-syn	4.464	5.93		$g_{\parallel}^* = 6.0$ $g_{\perp}^* = 3.5$	$H_{AN}$ 1/2	<1K Ferro	
$\text{dipy}_2\text{Co}_2(\mu\text{-OCCMe}_3)_2$ (OCCMe <sub>3</sub> ) <sub>2</sub> (dimer)	[59]	CoN <sub>2</sub> O <sub>4</sub> CoO <sub>5</sub> adjacent	(2) syn-syn	4.383	5.688			$H_H$ 3/2		
$[\text{Co}(3,4\text{-pyda})(\text{H}_2\text{O})_2]_n \cdot n\text{H}_2\text{O}$ (bilayer-dimer)	[23]	CoNO <sub>5</sub> CoO <sub>5</sub>	(1) syn-anti	4.773	4.39	8.3		$H_H$ 3/2		
$[\text{Co}\{\text{OOC}(\text{CH}_2)_{n-2}\text{-COO}\}(\text{H}_2\text{O})_2]$ d-12Co (chain)	[60,61]	CoO <sub>6</sub>	(1) anti-anti	5.93	6.0	−19.7		$H_I$ 1/2	−1.02	

Table 4. Cont.

	Ref.	Coord.	Exch. Path	Co-Co (Å)	C (emu·K/mol dimer)	$\theta$ (K)	g	Model Spin	J/k <sub>B</sub> (K)	D/k <sub>B</sub> (K)
[Co{CH <sub>3</sub> (CH <sub>2</sub> ) <sub>n-2</sub> COO} <sub>2</sub> (H <sub>2</sub> O) <sub>2</sub> ] m-12Co, m-20Co (chain)	[61]	CoO <sub>6</sub>	(1) anti-anti	6.3	7.0	-17.4 -31.8		H <sub>I</sub> 1/2	-0.65	
<b>Co-Co Carboxylate and Oxygen Mediated Exchange Paths</b>										
[Co <sub>2</sub> (H <sub>2</sub> O) <sub>4</sub> (Hbidc) <sub>2</sub> ] <sub>n</sub> (chain)	[62]	CoNO <sub>5</sub> outwards	(2) syn-syn (2) Co-O-Co	3.114	5.35	1	2.39	H <sub>H</sub> 3/2	1.21 Ferro	
{Co((κ <sub>1</sub> -κ <sub>1</sub> )-(κ <sub>1</sub> -μ <sub>2</sub> )-μ <sub>4</sub> TDC)(μ <sub>2</sub> H <sub>2</sub> O)0.5(H <sub>2</sub> O)} <sub>n</sub> (dimer)	[63]	CoO <sub>6</sub>	(2) syn-syn (1) Co-O-Co	3.212	7.06	2.63	g* = 5.2	H <sub>I</sub> 1/2		
bpyCo <sub>2</sub> (μ <sub>2</sub> -O,η <sub>2</sub> -OOCMe <sub>3</sub> ) (μ <sub>2</sub> -O,O'-OOCMe <sub>3</sub> ) <sub>2</sub> (η <sub>2</sub> -OOCMe <sub>3</sub> ) (unsymmetrical dimer)	[64]	CoNO <sub>5</sub> CoO <sub>5</sub>	(2) syn-syn (1) Co-O-Co	3.272					Ferro	
[Co <sub>2</sub> (μ-OAc) <sub>3</sub> (urea)(tmen) <sub>2</sub> ]- [OTf] (dimer)	[56]	CoN <sub>2</sub> O <sub>4</sub> adjacent	(2) syn-syn (1) Co-O-Co	3.4813	5.59		4.73 (dimer) (2 × 2.63)	H <sub>H</sub> L = 1	26	57
[Co <sub>2</sub> (μOAc)2(μ-AA)(urea) (tmen) <sub>2</sub> ][OTf] (3) (dimer)	[65,66]	CoN <sub>2</sub> O <sub>4</sub> adjacent	(2) syn-syn (1) Co-O-Co	3.4316	6.48		g <sub>  </sub> = 3.0 g <sub>⊥</sub> = 2.6 g <sub>av</sub> = 2.66	H <sub>H</sub> 3/2	-5.2	43
[Co <sub>2</sub> (μ-H <sub>2</sub> O)(μOAc) <sub>2</sub> (OAc) <sub>2</sub> (tmen) <sub>2</sub> ] (1) (dimer)	[65–67]	CoN <sub>2</sub> O <sub>4</sub> adjacent	(2) syn-syn (1) Co-O-Co	3.597	6.42	-8.5	g <sub>  </sub> = 2.9 g <sub>⊥</sub> = 2.5 g <sub>av</sub> = 2.64	H <sub>H</sub> 3/2	-1	64.3
[Co <sub>2</sub> (μ-OAc) <sub>2</sub> (OAc) <sub>2</sub> (μ-H <sub>2</sub> O) (phen) <sub>2</sub> ] (dimer)	[68]	CoN <sub>2</sub> O <sub>4</sub> adjacent		3.57	6.5					
[Co <sub>3</sub> (OH) <sub>2</sub> (3,4-pyda) <sub>2</sub> (H <sub>2</sub> O) <sub>2</sub> ] <sub>n</sub>	[23]	CoNO <sub>5</sub> CoO <sub>6</sub>	(1) syn-syn (1) Co-O-Co	2.988				H <sub>H</sub> 3/2	-8.3	

Table 4. Cont.

	Ref.	Coord.	Exch. Path	Co-Co (Å)	C (emu·K/mol dimer)	θ (K)	g	Model Spin	J/k <sub>B</sub> (K)	D/k <sub>B</sub> (K)
Co <sub>2</sub> (H <sub>2</sub> O)(C <sub>6</sub> H <sub>4</sub> O <sub>2</sub> N) <sub>4</sub> ·0.5CH <sub>3</sub> - CH <sub>2</sub> OH·0.5H <sub>2</sub> O (1) (dimer)	[22]	CoN <sub>2</sub> O <sub>4</sub>	(1) syn-syn (1) Co-O-Co		3.17	−31.2	2.53	H <sub>H</sub> 3/2	−7.9	
Co <sub>2</sub> (H <sub>2</sub> O)(C <sub>6</sub> H <sub>4</sub> O <sub>2</sub> N) <sub>4</sub> ·C <sub>6</sub> H <sub>5</sub> CH <sub>2</sub> OH (dimer)	[22]	CoN <sub>2</sub> O <sub>4</sub>	(1) syn-syn (1) Co-O-Co		3.42	−33.1	2.63	H <sub>H</sub> 3/2	−8.3	
{[Co(dpyo)(tp)(H <sub>2</sub> O) <sub>2</sub> ] [Co(H <sub>2</sub> O) <sub>6</sub> ](tp)(H <sub>2</sub> O)] <sub>n</sub> (chain) <b>Co-Co Oxalate Exchange Path</b>	[69]	CoO <sub>6</sub>	(1) syn-syn (1) Co-O-Co	3.742	6.56			H <sub>I</sub> 1/2	−12.4	
Na <sub>2</sub> Co <sub>2</sub> (C <sub>2</sub> O <sub>4</sub> ) <sub>3</sub> (H <sub>2</sub> O) <sub>2</sub> (2 LL-dimer)	[57], [70–72]	CoO <sub>6</sub>	(2) oxalate Co-O-C-O-C	5.393	4.86	−36	g <sub>x</sub> <sup>*</sup> = 2.8 g <sub>y</sub> <sup>*</sup> = 3.3 g <sub>z</sub> <sup>*</sup> = 5.75	H <sub>AN</sub> 1/2	−30.5 e <sub>x</sub> = 0.31 e <sub>y</sub> = 038	
[Co <sub>2</sub> (ox)tpmc](ClO <sub>4</sub> ) <sub>2</sub> ·3H <sub>2</sub> O (asymmetric dimer)	[73]	CoN <sub>4</sub> O <sub>2</sub>	(2) oxalate				g <sub>a</sub> = 3.42 g <sub>b</sub> = 4.02	H <sub>H</sub> 3/2	−12.9	6.6
“	[74]	“	“				g <sub>a</sub> <sup>*</sup> = 4.43 g <sub>b</sub> <sup>*</sup> = 3.12	H <sub>I</sub> 1/2	−16	

The local coordination in **1** is a distorted octahedron  $\text{CoN}_2\text{O}_4$ , with four oxygen atoms in the equatorial plane and two apical N atoms, which gives rise to a positive anisotropy constant  $D/k_B = 82$  K with an orthorhombic component  $E/D = 0.13$ . The most similar cases, from the viewpoint of the coordination and bridging paths are  $[\text{Co}(\text{Htatb})(\text{bimbp})].\text{DMF}$ , and  $[\text{Co}(\text{Htatb})(1\text{-}3\text{-bimbp})].\text{DMF}$  [54]. The three compounds have just 2 Co-O-C-O-Co syn-syn bridges, giving rise to an exchange interaction constant ranging between  $J/k_B = -6.65$  and  $-2.3$  K, that is, a weak antiferromagnetic interaction. No information on their single-ion anisotropy is available on the latter two cases. The other compounds with two or one carboxylate bridges also depict a different Co coordination, either with two N atoms, one adjacent to the other, or all oxygen atoms. The exchange interaction decays strongly in those compounds in comparison to the present compound.

It is of some interest to mention the compound  $\text{Co}_2(\text{esp})_2(\text{EtOH})_2$ , with a very different coordination, namely fourfold pyramidal, with the ligand at the apex. In contrast to all other cases, its anisotropy constant  $D < 0$ , i.e., axial easy axis. The Co-Co distance is very short, probably indicating the presence of a contribution from direct metal-metal interaction to the exchange interaction. Additionally, it supports four carboxylate bridges. Both contributions generate an AF exchange of  $J/k_B = -9.49$  K [55].

In stark contrast, the compounds with one or two oxygen mediated paths have ferro- or antiferromagnetic exchange, as high as  $J/k_B = 26$  K in  $[\text{Co}_2(\mu\text{-OAc})_3(\text{urea})(\text{tmen})_2][\text{OTf}]$  [56]. Thus, the oxygen mediated bridge may modify substantially the Co-Co interaction.

We have also included a last class of selected dimers, with oxalate bridging ligand, for comparison purposes. As said above, in the present work the magnetic properties of  $\{[\text{CoCxApy}] \cdot 2.15\text{H}_2\text{O}\}_n$  have been interpreted in terms of a two-legged ladder with predominant antiferromagnetic intra-rung interaction and with negligible intra-leg interaction. A similar conclusion was found in the compound  $\text{Na}_2\text{Co}_2(\text{C}_2\text{O}_4)_3(\text{H}_2\text{O})_2$ , where anisotropic  $\text{Co}^{2+}$  ions form a  $S = 1/2$  ladder, albeit with antiferromagnetic rung interaction; after neutron inelastic scattering experiments proved the predominance of the dimeric character of the dispersion relation [57]. At low temperature the anisotropic exchange Hamiltonian is applied, with a relatively strong intra-rung interaction  $J/k_B = -30.5$  K, and an exchange anisotropy of  $J_{x,y}/J \cong 0.35$  K. This case is of interest since the authors have applied the same approach as we have done in  $\{[\text{CoCxApy}] \cdot 2.15\text{H}_2\text{O}\}_n$ .

In Table 5 we have shortlisted the reported Co(II) dimers which entail SMM behavior. To be noticed is that there is no example of a Co(II) dimer showing slow relaxation at  $H = 0$ . Only some Co(II) dimers show slow magnetic relaxation under a field, and remarkably, all previously reported, have intradimer ferromagnetic exchange. Thus, to our knowledge, the present compound is the first Co(II) antiferromagnetically coupled dimer showing slow relaxation of the magnetization.

**Table 5.** Co-Co dimers with slow magnetic relaxation. Reference. Co coordination. Bridges (number) type. Co-Co distance.  $J$  exchange constant in  $S = 3/2$  Heisenberg isotropic model ( $H_H = -2J\mathbf{S}_1 \cdot \mathbf{S}_2$ ).  $D$ - Uniaxial anisotropy constant.  $H$  – Field applied to observe relaxation.  $\tau_0$  and  $U_{\text{eff}}$ - Arrhenius law parameters for Orbach magnetic relaxation.  $n$  and  $C$  Raman process parameters.

Compound	Ref.	Coord.	Bridges	Co-Co (Å)	$J/k_B$ (K)	$D/k_B$ (K)	$H$ (kOe)	$\tau_0$ (s)	$U_{\text{eff}}/k_B$ (K)	$n$	$C/K^{-n}$ (s <sup>-1</sup> )
[(dmso)CoL <sup>2</sup> ( $\mu$ -( <i>m</i> -NO <sub>2</sub> )C <sub>6</sub> H <sub>4</sub> COO)Co(NCS)] (2) symmetric	[75]	CoN <sub>2</sub> O <sub>4</sub> CoNO <sub>5</sub>	(2)Co-O-Co (1)Nitrobenzoate	2.98(2)	6.52	11.7 −1.86	3	$6.7 \times 10^{-13}$	31.3		
[Co <sub>2</sub> (bedmpzp) <sub>2</sub> ( $\mu$ -Cl) <sub>2</sub> ](PF <sub>6</sub> ) <sub>2</sub>	[76]	CoN <sub>4</sub> Cl <sub>2</sub>	(2) Co-Cl-Co	4.0061	2.0	273	5	Yes No data	Yes No data		
[CoCl <sub>2</sub> LC <sup>7</sup> ] (2)	[77]	CoN <sub>3</sub> Cl <sub>2</sub>	$\pi$ - $\pi$ contacts	5.662	1.03	219	2	$1.07 \times 10^{-7}$	14.6		
[CoCl <sub>2</sub> LC <sup>14</sup> ] (5)	[77]	CoN <sub>3</sub> Cl <sub>2</sub>	$\pi$ - $\pi$ contacts	4.515	0.76	125	2	$5.96 \times 10^{-8}$	40.5		
[Co <sub>2</sub> (pypz) <sub>2</sub> ( $\mu$ 1,1-N <sub>3</sub> ) <sub>2</sub> (N <sub>3</sub> ) <sub>2</sub> ].2CH <sub>3</sub> OH	[78]	CoN <sub>6</sub>	(2) Co-N-Co	3.3417	12.8	2.14	3	HF $5.15 \times 10^{-15}$ LF 1.5	95	1.6	412
{[CoC <sub>x</sub> APy]}.2.15 H <sub>2</sub> O} <sub>n</sub> (2 LL-dimer)	This work	CoN <sub>2</sub> O <sub>4</sub> apical	(2) syn-syn carboxylate	3.9684	−0.45	<sup>82</sup> $E/D = 0.13$	5	HF $1.9 \times 10^{-6}$ LF 2.0	6.7		

At zero magnetic field we do not observe spin relaxation of the magnetization within our frequency experimental window. This result may indicate that spin relaxation is very fast, and we are observing the isothermal susceptibility, what could be explained as due to a strong spin coupling through hyperfine interactions. The nuclear moment  $I = 7/2$  of  $^{59}\text{Co}$  couples with the  $S^* = 1/2$  ground state dimer levels leading to the opening of new relaxation paths. A sizable Van Vleck susceptibility ensues giving rise to nearly frequency independent  $\chi'$  susceptibility. As the magnetic field increases there is a continuous crossover giving the states a net magnetic moment that makes them detectable by magnetic susceptibility measurements. Therefore, slow relaxation can be observed under a magnetic field of sufficient intensity. This mechanism is described for a single Co(II) ion [79]. However, it necessarily is also taking place in the dimer; in our antiferromagnetically coupled dimer model, we are dealing with a singlet ground state with zero expected magnetic moment for  $H = 0$ . A small ac magnetic field would induce a reversible build-up of magnetic moment by modulating the electronuclear wave function, in a so called Van Vleck susceptibility component. This component does not drive the spin system out of equilibrium and therefore does not contribute to spin relaxation processes.

As a magnetic field is applied, the dominant AF interaction and the anisotropy in the interaction gives as the result four levels with a weak dependence with the applied field (see Figure 2d). This would explain the need for a rather large field to show a sizeable change, and the appearance of slow relaxation processes for fields above 1.2 kOe.

On the other hand, in order to gain insight into the spin relaxation phenomena we analyzed the relative weight of the different observed processes. If we take a closer look at the ac susceptibility variation with the magnetic field at  $T = 2$  K, it is remarkable the strong variation of the adiabatic susceptibility of the slow frequency process, which is determined by the  $\chi'$  at 100 Hz,  $\chi_{\infty}^{\text{lf}}$  (see Supplementary Materials, Figures S11 and S12). This is explained by the fact that the larger the field, the more dominant is this process with respect to the reversible susceptibility contribution, as more effective moment is grown in the ground state. For  $H = 5$  kOe, 22% of the magnetic susceptibility is blocked for frequencies larger than 1 Hz, which increases to a 52% for 10 kOe. We have assigned this long relaxation time process to a direct process.

It is worthy to note that in our complex the dimers are assembled in 2 leg infinite ladders (2LL) along the  $c$ -axis. This configuration makes this compound a potential candidate as a physical realization of a 1D Haldane gap system, for which interesting theoretical predictions have been made [80].

We have demonstrated that in the investigated temperature range (down to 1.9 K) the static and dynamic magnetic data may be rationalized in terms of a dimeric model of Co-Co with intra-rung interaction, with negligible leg-interaction.

Nevertheless, it is plausible that at lower temperatures intra-leg interactions would start to be relevant, and manifest in the way the magnetic susceptibility decays as temperature decreases towards  $T = 0$ . Indeed, at low temperatures, the magnetic sublattice can be modelled as a 2LL  $S = 1/2$  symmetric ladder, with the Co-Co rung-interaction,  $J_{\perp}$ , and the intra-leg interaction,  $J_{\parallel}$ . The magnitude and sign of the ratio  $J_{\perp}/J_{\parallel}$  determine a large variety of collective magnetic behavior ( $J_{\perp} < 0$ , [81]  $J_{\perp} > 0$  [82]). Of importance is whether the ladder is a Haldane gap system, since in that case the magnetic susceptibility approaches zero at  $T = 0$  in the Haldane gapped model, while the magnetic susceptibility decreases to finite values in the case of no-gap.

In terms of the ladder model, the present case corresponds to approximately  $J_{\perp}/J_{\parallel} \rightarrow +\infty$ , where  $J_{\perp}$  has AF character. In Shelton et al. 1996 [83], it was shown that a  $S = 1/2$ , 2LL spin-ladder always has a spin-gap irrespective of the sign of  $J_{\perp}$ , and proportional to it. In the  $J_{\perp} < 0$  (AF case), the ground state is a singlet, and the ladder excited band is the dimer  $S = 1$  triplet with a width  $\approx J_{\parallel}$ . In the  $J_{\perp} > 0$  (FM case), the ground state is a triplet, and the system behaves as a  $S = 1$  linear chain, and, therefore, has a Haldane spin-gap.

Therefore, in view of the anisotropic interaction and the topology, this complex may result in a particular and interesting realization of a Haldane gap. For the study of this

model, and their interesting theoretical predictions, we would need to go down to much lower temperatures ( $T < 0.4$  K), where AF interdimer interaction along the 2LL may start to play a role as the kinetic energy becomes of the order of the leg weak interaction.

## 4. Materials and Methods

### 4.1. Experimental Techniques

Fourier transform infrared (FTIR) spectra were recorded using a Bruker Vertex 70 FTIR spectrometer. Registrations were performed in the transmission mode in the range  $400\text{--}4000\text{ cm}^{-1}$  at room temperature with a resolution of  $2\text{ cm}^{-1}$  and accumulation of 32 scans. UV-Vis absorption spectra measurements were carried out in DMF solution on a Specord 200 spectrophotometer. Carbon, hydrogen, and nitrogen content were determined on a Perkin–Elmer CHNS 2400 II elemental analyzer. Energy-dispersive X-ray spectroscopy (EDX) system available on the Quanta 200 scanning electron microscope (FEI company, Brno, Czech Republic) and X-ray fluorescence (EDXRF) system EX-2600 X-Calibur SDD (Xenometrix, Migdal HaEmek, Israel) were used to estimate the Zn:Co molar ratio in compound **2**. The thermogravimetric analyses were performed on a STA 449F1 Jupiter NETZSCH (Germany) equipment within  $20\text{--}700\text{ }^{\circ}\text{C}$  under a nitrogen flow ( $50\text{ mL/min}$ ) using a heating rate of  $10\text{ }^{\circ}\text{C/min}$ , taking  $10\text{ mg}$  sample. Alumina crucible was used as sample holder. Differential scanning calorimetry (DSC) measurements were conducted on a DSC 200 F3 Maia (Netzsch, Germany) at a heating/cooling rate of  $10\text{ }^{\circ}\text{C/min}$  in nitrogen used as inert atmosphere at a flow rate of  $100\text{ mL/min}$ .

X-ray diffraction data for **1** and **2** were collected with an Oxford-Diffraction XCAL-IBUR E CCD diffractometer equipped with graphite-monochromated  $\text{MoK}\alpha$  radiation. The experimental data comprise 383 and 388 frames each for 5 and 180 s over  $1^{\circ}$  oscillation width and crystal-to-detector distance at  $40\text{ mm}$ . The unit cell determination and data integration were carried out using the CrysAlis package of Oxford Diffraction [84]. The structure was solved by direct methods using Olex2.77 software with the SHELXS structure solution program and refined by full-matrix least-squares on  $F^2$  with SHELXL-2015 [85]. Hydrogen atoms were inserted in fixed, idealized positions and refined as rigidly bonded to the corresponding non-hydrogen atoms. The positional parameters for H-atoms of OH groups were determined from Fourier maps and refined according to H-bonds parameters. Identical positional parameters and displacement parameters were assumed for Co and Zn atoms in the crystal **2**. When the occupancy factors for Co and Zn atoms were allowed to be refined, a conclusive ratio of 0.82:0.18 has resulted. The molecular plots were obtained using the Olex2 program. Crystal data and some further details concerning X-ray analysis are given in Table 1. The bond lengths and angles for **1** and **2** are listed in Tables S2 and S3, CCDC- 2005545, 2005606. These data can be obtained free of charge via [www.ccdc.cam.ac.uk/conts/retrieving.html](http://www.ccdc.cam.ac.uk/conts/retrieving.html) (or from the Cambridge Crystallographic Data Centre, 12 Union Road, Cambridge CB2 1EZ, UK; Fax: (+44) 1223-336-033; or structure@ccdc.ca.ac.uk). Powder X-ray diffractogram was recorded on a Rigaku Miniflex 600 diffractometer (Tokyo, Japan) using  $\text{CuK}\alpha$ -emission in the angular range of  $10\text{--}60$  ( $2\theta$ ) with a scanning step of  $0.01^{\circ}$  and a recording rate of  $1^{\circ}/\text{min}$ .

Electron Paramagnetic Resonance (EPR) measurements were conducted in a ELEXYS E580E spectrometer from Bruker. A liquid helium refrigerated Oxford CF900 continuous-flow cryostat was employed for measurements at low temperatures. The powdered polycrystalline sample was dispersed in n-hexane and introduced in a quartz tube (707-SQ from Wilmad Labglass). The sample was cooled at zero field to avoid preferential orientation in the field.

Static magnetic measurements, magnetization,  $M(H)$ , and susceptibility,  $\chi(T)$ , data were collected from polycrystalline samples, embedded in Daphne Oil or n-Hexane to avoid grain orientation, in a Quantum Design SQUID Magnetometer equipped with the RSO option and a Quantum Design PPMS with the VSM option.  $M(H)$  was measured at  $T = 2.0\text{ K}$  up to  $140\text{ kOe}$  and  $\chi(T)$  from  $1.9$  to  $300\text{ K}$ , with an applied field of  $1\text{ kOe}$ . Heat capacity under different applied fields ( $0\text{--}30\text{ kOe}$ ) was measured down to  $0.35\text{ K}$  on a

pressed powder pellet fixed with Apiezon N grease, using the same PPMS equipped with a  $^3\text{He}$  refrigerator.

Dynamic magnetic measurements for polycrystalline samples were done at fixed temperatures in the range  $1.8 < T < 6$  K, with an excitation field of 4 Oe, at dc bias fields in the range  $0 < H < 50$  kOe, while sweeping the frequency  $0.1 < f < 10,000$  Hz. Low frequency range (0.1 Hz–1 KHz) was measured with a SQUID magnetometer, and high frequency range (10 Hz–10 kHz) with the ACMS magnetometer option of the PPMS.

#### 4.2. Materials

1,3-Bis(3-carboxypropyl)tetramethyldisiloxane ( $\text{H}_2\text{Cx}$ ),  $[\text{HOOC}(\text{CH}_2)_3(\text{CH}_3)_2\text{Si}]_2\text{O}$ , MW = 306.5 was prepared according to already published procedure [86], while 4,4'-azopyridine (APy),  $\text{C}_{10}\text{H}_8\text{N}_4$ , MW = 184.20, Cobalt(II) perchlorate hexahydrate,  $\text{Co}(\text{ClO}_4)_2 \cdot 6\text{H}_2\text{O}$ , MW = 365.93 and Zinc perchlorate hexahydrate,  $\text{Zn}(\text{ClO}_4)_2 \cdot 6\text{H}_2\text{O}$ , MW = 372.38, 2,6-Dimethylpyridine,  $\text{C}_7\text{H}_9\text{N}$ , MW = 107.15, and ethanol were purchased from Sigma-Aldrich.

##### 4.2.1. Preparation of $\{[\text{CoCxAPy}]\cdot 2.15 \text{H}_2\text{O}\}_n$ (1)

1,3-Bis(3-carboxypropyl)tetramethyldisiloxane, Cx, (0.150 g, 0.49 mmol) was mixed with 4,4'-azopyridine, APy, (0.090 g, 0.49 mmol) in 10 mL ethanol. The mixture was stirred 20 min and, after adding 2,6-dimethylpyridine (0.053 g, 0.49 mmol), was heated to reflux for one hour. After cooling to room temperature, this mixture was filtered and added by layering on the walls of the glass tube containing a solution of 0.360 g (0.98 mmol)  $\text{Co}(\text{ClO}_4)_2 \cdot 6\text{H}_2\text{O}$  dissolved in 15 mL distilled water. It was left to rest at room temperature. In these conditions, a crystalline compound **1** is obtained; Yield: 0.178 g, 31% based on Co content, separated from the reaction mixture after more than two weeks. Elem. anal., wt%: Calcd. for  $\text{C}_{22}\text{H}_{36.3}\text{CoN}_4\text{O}_{7.15}\text{Si}_2$  (MW = 586.36): C 45.06, H 6.24, N 9.56. Found: C 44.93, H 6.50, N 9.98. IR  $\nu_{\text{max}}$  (KBr),  $\text{cm}^{-1}$ : 3545 s, 3418 s, 3105 w, 2953 m, 2922 m, 2895 m, 2872 w, 1724 w, 1601 s, 1555 vs, 1483 w, 1447 s, 1425 s, 1385 s, 1319 m, 1254 s, 1225 m, 1124 w, 1083 s, 1047 vs, 1016 s, 876 w, 839 s, 795 s, 748 w, 700 w, 665 w, 623 s, 585 w, 571 m, 549 w, 527 w.

##### 4.2.2. Preparation of $\{[\text{Zn}_{0.80}\text{Co}_{0.2}\text{CxAPy}]\cdot 1.5 \text{CH}_3\text{OH}\}_n$ (2)

Compound **2**, wherein Co was largely replaced by zinc was prepared under similar conditions but in methanol as a solvent (10 mL) and using a mixture  $\text{Co}(\text{ClO}_4)_2 \cdot 6\text{H}_2\text{O}$ :  $\text{Zn}(\text{ClO}_4)_2 \cdot 6\text{H}_2\text{O}$  at molar ratio 5:95, namely 0.018 g (0.05 mmol)  $\text{Co}(\text{ClO}_4)_2 \cdot 6\text{H}_2\text{O}$  and 0.354 g (0.95 mmol)  $\text{Zn}(\text{ClO}_4)_2 \cdot 6\text{H}_2\text{O}$ , the quantities of the other reactants and procedure remaining the same as in the recipe of compound **1**; Yield: 0.026 g, 17% based on Co content. Elem. anal., wt%: Calcd. for  $\text{C}_{23.5}\text{H}_{38}\text{Co}_{0.2}\text{N}_4\text{O}_{6.5}\text{Si}_2\text{Zn}_{0.8}$  (MW = 600.81): C 46.98, H 6.38, N 9.33. Found: C 45.50, H 6.24, N 9.78. Co:Zn molar ratio: 0.22:0.78 (EDX), 0.21:0.79 (XRF); IR  $\nu_{\text{max}}$  (KBr),  $\text{cm}^{-1}$ : 3437 m, 3105 vw, 3076 vw, 3044 vw, 2953 m, 2922 m, 2893 m, 2870 w, 2795 vw, 1713 w, 1601 vs, 1553 vs, 1481 w, 1445 s, 1423 s, 1339 w, 1317 m, 1254 s, 1223 m, 1165 w, 1126 m, 1045 vs, 1016 s, 968 w, 880 w, 837 s, 795 s, 744 m, 700 m, 663 w, 606 w, 571 m, 548 m, 528 m.

## 5. Conclusions

The synthesis, structure, and magnetic properties of a new MOF compound,  $\{[\text{CoCxAPy}]\cdot 2.15 \text{H}_2\text{O}\}_n$ , built from the stacking of 2D CPs formed by the adjacent bonding of ladders with dimer Co-rungs have been reported. A multitechnique approach, based on EPR, heat capacity, and magnetic characterization, together with *ab initio* calculations, has allowed the unequivocal determination of the magnetic model and the exchange coupling scheme. Single-ion Co(II) in this compound is described by two KD's separated 166 K in energy, where the  $M_S = \pm 1/2$  doublet is stabilized as ground state with effective gyromagnetic factors  $g_x^* = 4.07$ ,  $g_y^* = 5.57$ , and  $g_z^* = 1.944$ . Co(II) ions form magnetic dimers with anisotropic AF exchange parameters,  $J_x^*/k_B = -0.5 \pm 0.05$  K,  $J_y^*/k_B = -2.3 \pm 0.3$  K, and  $J_z^*/k_B = -0.5 \pm 0.05$  K. The degree of anisotropy in the magnetic exchange is of similar

magnitude as the anisotropy of the Co(II) single-ion ground state. The Co(II) dimer shows SMM behavior under applied magnetic field. Two different magnetic relaxation processes show up, a slow  $\tau_f \approx 2$  s direct process and an Orbach process at higher frequencies with  $U/k_B = 6.7 \pm 0.5$  K. Slow relaxation processes involve uniquely dimer energy levels. The new compound represents a rare instance of a MOF built up from ladders showing SMM of the dimeric Co-rungs.

**Supplementary Materials:** Supplementary Information (SI). In section SI1, we provide additional crystal data and structure information. Figure S1: FTIR spectra for the compounds **1** and **2**. Figure S2: Thermogravimetric curves. Table S1: Main thermal decomposition steps of compounds **1** and **2**. Figure S3: EDX spectrum for compound **2**. Figure S4: XRF spectrum for compound **2**. Figure S5: DSC curves for compound **1**. Figure S6: PXRD diffractograms of the compounds **1** and **2** at room temperature. Table S2: Bond distances and angles for **1**. Figure S7: View of the asymmetric unit of coordination polymer **2**. Figure S8. View of the 2D MOF in the crystal structure of **2**. Table S3: Bond distances and selected angles for **2**. In the following sections (SI2, SI3 and SI4), we provide additional information about the magnetic properties of the studied compounds. Figure S9: Temperature dependence of the  $\chi \cdot T$  product for pure **1** and diluted compound **2** showing the high temperature fit to a Curie-Weiss law with parameters of Table 2 in the main text. Figure S10: Magnetic entropy per Co(II) ion as a function of temperature for different applied magnetic fields. Figure S11: In-phase component of the ac magnetic susceptibility as a function of frequency. Figure S12: In-phase amplitude of the low frequency process at  $T = 2$  K as a function of the applied dc magnetic field.

**Author Contributions:** Conceptualization, M.C., C.T., J.B., E.B. and A.A.; methodology, S.S., J.B.; software, J.L. and A.A.; validation, A.A. and S.S.; formal analysis, A.A., E.B., J.L. and P.J.A.; investigation, A.A., P.J.A., M.F.Z. and A.V.; writing—original draft preparation, A.A.; writing—review and editing, A.A., M.C., S.S., J.B., E.B., P.J.A. and J.L.; funding acquisition, M.C. All authors have read and agreed to the published version of the manuscript.

**Funding:** This research was funded by the Spanish Ministry of Economy, Industry, and Competitiveness (MINECO, Grant No. MAT2017-83468-R), by the Spanish Ministry of Science, Innovation, and Universities (MICIU, Grant No. PGC-2018–099024-B100) and by the regional Government of Aragon (E12-20R RASMIA project). This work was supported by a grant of the Romanian Ministry of Education and Research, CNCS -UEFISCDI, project number PN-III-P4-ID-PCE-2020-2000, within PNCDI III, Contract 207/2020 (2D-PerMONSil).

**Institutional Review Board Statement:** Not applicable.

**Informed Consent Statement:** Not applicable.

**Data Availability Statement:** Data supporting reported results can be provided by the corresponding author A.A. upon request.

**Acknowledgments:** Authors would like to acknowledge the use of Servicio General de Apoyo a la Investigación-SAL, Universidad de Zaragoza.

**Conflicts of Interest:** The authors declare no conflict of interest. The funders had no role in the design of the study; in the collection, analyses, or interpretation of data; in the writing of the manuscript, or in the decision to publish the results.

## References

1. Suh, M.P.; Park, H.J.; Prasad, T.K.; Lim, D.-W. Hydrogen storage in metal-organic frameworks. *Chem. Rev.* **2012**, *112*, 782–835. [[CrossRef](#)]
2. Sumida, K.; Rogow, D.L.; Mason, J.A.; McDonald, T.M.; Bloch, E.D.; Herm, Z.R.; Bae, T.H.; Long, J.R. Carbon dioxide capture in metal-organic frameworks. *Chem. Rev.* **2012**, *112*, 724–781. [[CrossRef](#)] [[PubMed](#)]
3. Halder, G.J.; Kepert, C.J.; Moubaraki, B.; Murray, K.S.; Cashion, J.D. Guest-dependent spin crossover in a nanoporous molecular framework material. *Science* **2002**, *298*, 1762–1765. [[CrossRef](#)] [[PubMed](#)]
4. Li, J.R.; Sculley, J.; Zhou, H.-C. Metal–Organic Frameworks for Separations. *Chem. Rev.* **2012**, *112*, 869–932. [[CrossRef](#)]
5. Yoon, M.; Srirambalaji, R.; Kim, K. Homochiral Metal–Organic Frameworks for Asymmetric Heterogeneous Catalysis. *Chem. Rev.* **2011**, *112*, 1196–1231. [[CrossRef](#)]
6. Bartolomé, E.; Alonso, P.J.; Arauzo, A.; Luzón, J.; Bartolomé, J.; Racles, C.; Turta, C. Magnetic properties of the seven-coordinated nanoporous framework material Co(bpy)1.5(NO3)2 (bpy = 4,4'-bipyridine). *Dalton Trans.* **2012**, *41*, 10382. [[CrossRef](#)]

7. Sun, L.; Campbell, M.G.; Dincă, M. Electrically Conductive Porous Metal-Organic Frameworks. *Angew. Chem. Int. Ed.* **2016**, *55*, 3566–3579. [[CrossRef](#)] [[PubMed](#)]
8. Zhao, S.-N.; Wang, G.; Poelman, D.; Van Der Voort, P. Luminescent Lanthanide MOFs: A Unique Platform for Chemical Sensing. *Materials* **2018**, *11*, 572. [[CrossRef](#)]
9. Xie, Z.; Xu, W.; Cui, X.; Wang, Y. Recent Progress in Metal-Organic Frameworks and Their Derived Nanostructures for Energy and Environmental Applications. *ChemSusChem* **2017**, *10*, 1645–1663. [[CrossRef](#)] [[PubMed](#)]
10. Wang, B.; Jin, J.; Ding, B.; Han, X.; Han, A.; Liu, J. General Approach to Metal-Organic Framework Nanosheets With Controllable Thickness by Using Metal Hydroxides as Precursors. *Front. Mater.* **2020**, *7*, 37. [[CrossRef](#)]
11. Espallargas, G.M.; Coronado, E. Magnetic functionalities in MOFs: From the framework to the pore. *Chem. Soc. Rev.* **2017**, *47*, 533–557. [[CrossRef](#)]
12. Miyasaka, H.; Nakata, K.; Sugiura, K.-i.; Yamashita, M.; Clerac, R. A three-dimensional ferrimagnet composed of mixed-valence Mn<sup>4+</sup> clusters linked by an [Mn<sub>4</sub>N(CN)<sub>2</sub>]<sub>6</sub> unit. *Angew. Chem. Int. Ed.* **2004**, *43*, 707–711. [[CrossRef](#)]
13. Oyarzabal, I.; Fernández, B.; Cepeda, J.; Gómez-Ruiz, S.; Calahorra, A.J.; Seco, J.M.; Rodríguez-Diéguez, A. Slow relaxation of magnetization in 3D-MOFs based on dysprosium dinuclear entities bridged by dicarboxylic linkers. *CrystEngComm* **2016**, *18*, 3055–3063. [[CrossRef](#)]
14. Vallejo, J.; Fortea-Pérez, F.R.; Pardo, E.; Benmansour, S.; Castro, I.; Krzystek, J.; Armentano, D.; Cano, J. Guest-dependent single-ion magnet behaviour in a cobalt(ii) metal-organic framework. *Chem. Sci.* **2015**, *7*, 2286–2293. [[CrossRef](#)] [[PubMed](#)]
15. Kurmoo, M. Magnetic metal-organic frameworks. *Chem. Soc. Rev.* **2009**, *38*, 1353–1379. [[CrossRef](#)] [[PubMed](#)]
16. Rechkemmer, Y.; Breitgoff, F.D.; Van Der Meer, M.; Atanasov, M.; Hakl, M.; Orlita, M.; Neugebauer, P.; Neese, F.; Sarkar, B.; Van Slageren, J. A four-coordinate cobalt(II) single-ion magnet with coercivity and a very high energy barrier. *Nat. Commun.* **2016**, *7*, 10467. [[CrossRef](#)]
17. Chen, L.; Zhao, W.; Yi, G.; Zhou, J.; Yuan, A. Single-Ion Magnets based on 3d metals. *Prog. Chem.* **2019**, *31*, 337–350.
18. Kostakis, G.E.; Perlepes, S.P.; Blatov, V.A.; Proserpiod, D.; Powell, A.K. High-nuclearity cobalt coordination clusters: Synthetic, topological and magnetic aspects. *Coord. Chem. Rev.* **2012**, *256*, 1246–1278. [[CrossRef](#)]
19. Konieczny, P.; Gonzalez-Guillén, A.B.; Luberd-Durnaś, K.; Čížmár, E.; Peřka, R.; Oszejca, M.; Łasocha, W. 1D coordination polymer (OPD)<sub>2</sub>CoII(SO<sub>4</sub>) showing SMM behaviour and multiple relaxation modes. *Dalton Trans.* **2019**, *48*, 7560–7570. [[CrossRef](#)] [[PubMed](#)]
20. Wang, M.; Gou, X.; Shi, W.; Cheng, P. Single-chain magnets assembled in cobalt(ii) metal-organic frameworks. *Chem. Commun.* **2019**, *55*, 11000–11012. [[CrossRef](#)]
21. Brunet, G.; Safin, D.A.; Jover, J.; Ruiz, E.; Murugesu, M. Single-molecule magnetism arising from cobalt(ii) nodes of a crystalline sponge. *J. Mater. Chem. C* **2016**, *5*, 835–841. [[CrossRef](#)]
22. Liu, Y.-H.; Tsai, H.-L.; Lu, Y.-L.; Wen, Y.-S.; Wang, J.-C.; Lu, K.-L. Assembly of a Robust, Thermally Stable Porous Cobalt(II) Nicotinate Framework Based on a Dicobalt Carboxylate Unit. *Inorg. Chem.* **2001**, *40*, 6426–6431. [[CrossRef](#)] [[PubMed](#)]
23. Tong, M.-L.; Kitagawa, S.; Chang, H.-C.; Ohba, M. Temperature-controlled hydrothermal synthesis of a 2D ferromagnetic coordination bilayered polymer and a novel 3D network with inorganic Co<sub>3</sub>(OH)<sub>2</sub>ferrimagnetic chains. *Chem. Commun.* **2004**, *4*, 418–419. [[CrossRef](#)] [[PubMed](#)]
24. Goswami, S.; Leitus, G.; Tripuramallu, B.K.; Goldberg, I. MnII and CoII coordination polymers showing field-dependent magnetism and slow magnetic relaxation behavior. *Cryst. Growth Des.* **2017**, *17*, 4393–4404. [[CrossRef](#)]
25. Mariano, L.D.S.; Rosa, I.M.; De Campos, N.R.; Doriguetto, A.C.; Dias, D.F.; do Pim, W.D.; Valdo, A.K.S.; Martins, F.T.; Ribeiro, M.A.; De Paula, E.E.; et al. Polymorphic derivatives of NiII and CoII mesocates with 3D networks and ‘brick and mortar’ structures: Preparation, structural characterization, and cryomagnetic investigation of new single molecule magnets. *Cryst. Growth Des.* **2020**, *20*, 2462–2476. [[CrossRef](#)]
26. Cazacu, M.; Vlad, A.; Turta, C.; Lisa, G. New iron-cobalt clusters with silicon-containing dicarboxylic acids. *Open Chem.* **2012**, *10*, 1079–1086. [[CrossRef](#)]
27. Vlad, A.; Cazacu, M.; Zaltariov, M.F.; Shova, S.; Turta, C.; Airinei, A. Metallopolymeric structures containing highly flexible siloxane sequence. *Polymer* **2013**, *54*, 43–53. [[CrossRef](#)]
28. Nitschke, J. Construction, Substitution, and Sorting of Metallo-organic Structures via Subcomponent Self-Assembly. *Acc. Chem. Res.* **2006**, *40*, 103–112. [[CrossRef](#)]
29. Vlad, A.; Cazacu, M.; Zaltariov, M.F.; Barga, A.; Shova, S.; Turta, C. A 2D metal-organic framework based on dizinc coordination units bridged through both flexible and rigid ligands. *J. Mol. Struct.* **2014**, *1060*, 94–101. [[CrossRef](#)]
30. Shova, S.; Vlad, A.; Damoc, M.; Tiron, V.; Dascalu, M.; Novitchi, G.; Ursu, C.; Cazacu, M. Nanoscale Coordination Polymer of Dimanganese(II) as Infinite, Flexible Nanosheets with Photo-Switchable Morphology. *Eur. J. Inorg. Chem.* **2020**, *2020*, 2043–2054. [[CrossRef](#)]
31. Nakamoto, K. Infrared and Raman Spectra of Inorganic and Coordination Compounds. In *Handbook of Vibrational Spectroscopy*; Griffiths, P.R., Ed.; John Wiley & Sons, Ltd.: Chichester, UK, 2006.
32. Marnadu, R.; Chandrasekaran, J.; Vivek, P.; Balasubramani, V.; Maruthamuthu, S. Impact of Phase Transformation in WO<sub>3</sub> Thin Films at Higher Temperature and its Compelling Interfacial Role in Cu/WO<sub>3</sub>/p-Si Structured Schottky Barrier Diodes. *Z. Phys. Chem.* **2020**, *234*, 355–379. [[CrossRef](#)]

33. Liu, Y.; Zhang, G.; Haibibu, A.; Han, Z.; Wang, Q. High cyclic stability of electrocaloric effect in relaxor poly(vinylidene fluoride-trifluoroethylene-chlorofluoroethylene) terpolymers in the absence of ferroelectric phase transition. *J. Appl. Phys.* **2019**, *126*, 234102. [[CrossRef](#)]
34. Osaki, K.; Uryû, N. Anisotropic g-Factors of Co<sup>2+</sup> Ion in Complex Salts. *J. Phys. Soc. Jpn.* **1976**, *40*, 1575–1583. [[CrossRef](#)]
35. Bocca, R. Zero-field splitting in metal complexes. *Coord. Chem. Rev.* **2004**, *248*, 757–815. [[CrossRef](#)]
36. Pali, A.; Tsukerblat, B.; Clemente-Juan, J.M.; Coronado, E. Magnetic exchange between metal ions with unquenched orbital angular momenta: Basic concepts and relevance to molecular magnetism. *Int. Rev. Phys. Chem.* **2010**, *29*, 135–230. [[CrossRef](#)]
37. Malmqvist, P.; Roos, B.O. The CASSCF state interaction method. *Chem. Phys. Lett.* **1989**, *155*, 189–194. [[CrossRef](#)]
38. Angeli, C.; Cimraglia, R.; Evangelisti, S.; Leininger, T.; Malrieu, J.-P. Introduction of n-electron valence states for multireference perturbation theory. *J. Chem. Phys.* **2001**, *114*, 10252. [[CrossRef](#)]
39. Neese, F. The ORCA program system. *Wiley Interdiscip. Rev. Comput. Mol. Sci.* **2011**, *2*, 73–78. [[CrossRef](#)]
40. Neese, F. Software update: The ORCA program system, version 4.0. *Wiley Interdiscip. Rev. Comput. Mol. Sci.* **2018**, *8*, e1327. [[CrossRef](#)]
41. Pantazis, D.A.; Chen, X.-Y.; Landis, C.R.; Neese, F. All-Electron Scalar Relativistic Basis Sets for Third-Row Transition Metal Atoms. *J. Chem. Theory Comput.* **2008**, *4*, 908–919. [[CrossRef](#)] [[PubMed](#)]
42. Neese, F. An improvement of the resolution of the identity approximation for the formation of the Coulomb matrix. *J. Comput. Chem.* **2003**, *24*, 1740–1747. [[CrossRef](#)]
43. Izsak, R.; Neese, F. An overlap fitted chain of spheres exchange method. *J. Chem. Phys.* **2011**, *135*, 144105. [[CrossRef](#)] [[PubMed](#)]
44. Heß, B.A.; Marian, C.M.; Wahlgren, U.; Gropen, O. A mean-field spin-orbit method applicable to correlated wavefunctions. *Chem. Phys. Lett.* **1996**, *251*, 365–371. [[CrossRef](#)]
45. Neese, F. Efficient and accurate approximations to the molecular spin-orbit coupling operator and their use in molecular g-tensor calculations. *J. Chem. Phys.* **2005**, *122*, 034107. [[CrossRef](#)] [[PubMed](#)]
46. Stoll, S.; Schweiger, A. EasySpin, a comprehensive software package for spectral simulation and analysis in EPR. *J. Magn. Reson.* **2006**, *178*, 42–55. [[CrossRef](#)]
47. Pavlov, A.A.; Nehr Korn, J.; Pankratova, Y.A.; Ozerov, M.; Mikhalyova, E.A.; Polezhaev, A.V.; Nelyubina, Y.V.; Novikov, V.V. Detailed electronic structure of a high-spin cobalt(ii) complex determined from NMR and THz-EPR spectroscopy. *Phys. Chem. Chem. Phys.* **2019**, *21*, 8201–8204. [[CrossRef](#)] [[PubMed](#)]
48. Lazarescu, A.; Shova, S.; Bartolome, J.; Alonso, P.J.; Arauzo, A.; Balu, A.M.; Simonov, Y.A.; Gdaniec, M.; Turta, C.; Filoti, G.; et al. Heteronuclear (Co–Ca, Co–Ba) 2,3-pyridinedicarboxylate complexes: Synthesis, structure and physico-chemical properties. *Dalton Trans.* **2011**, *40*, 463–471. [[CrossRef](#)]
49. Pilbrow, J.R. Effective g values for S = 3/2 and S = 5/2. *J. Magn. Reson.* **1978**, *31*, 479–490. [[CrossRef](#)]
50. Bartolomé, E.; Arauzo, A.; Luzón, J.; Bartolomé, J.; Bartolomé, F. Magnetic Relaxation of Lanthanide-Based Molecular Magnets. In *Handbook of Magnetic Materials*; Elsevier B.V.: Amsterdam, The Netherlands, 2017; Volume 26, pp. 1–289.
51. Arauzo, A.; Bartolomé, E.; Benniston, A.C.; Melnic, S.; Shova, S.; Luzón, J.; Alonso, P.J.; Barra, A.-L.; Bartolomé, J. Slow magnetic relaxation in a dimeric Mn<sub>2</sub>Ca<sub>2</sub> complex enabled by the large Mn(III) rhombicity. *Dalton Trans.* **2016**, *46*, 720–732. [[CrossRef](#)]
52. Bleaney, B.; Ingram, D.J.E. Hyperfine structure of the paramagnetic resonance spectrum of divalent cobalt: Experimental. *Nature* **1949**, *164*, 116–117. [[CrossRef](#)]
53. Algra, H.A.; Greidanus, F.J.A.M.; de Jongh, L.J.; Huiskamp, W.J.; Reedijk, J. Hyperfine specific heats of two paramagnetic, octahedrally coordinated Co<sup>2+</sup> compounds. *Phys. B+C* **1976**, *83*, 85–91. [[CrossRef](#)]
54. Tang, L.; Wang, H.H.; Fu, Y.H.; Wang, Y.T.; Wang, J.; Hou, X. Three cobalt-based coordination polymers with tripodal carboxylate and imidazole-containing ligands: Syntheses, structures, properties and DFT studies. *RSC Adv.* **2019**, *9*, 38902–38911. [[CrossRef](#)]
55. Pakula, R.J.; Berry, J.F. Cobalt complexes of the chelating dicarboxylate ligand “esp”: A paddlewheel-type dimer and a heptanuclear coordination cluster. *Dalton Trans.* **2018**, *47*, 13887–13893. [[CrossRef](#)]
56. Ostrovsky, S.M.; Falk, K.; Pelikán, J.; Brown, D.A.; Tomkowicz, Z.; Haase, W. Orbital Angular Momentum Contribution to the Magneto-Optical Behavior of a Binuclear Cobalt(II) Complex. *Inorg. Chem.* **2006**, *45*, 688–694. [[CrossRef](#)] [[PubMed](#)]
57. Matsuda, M.; Wakimoto, S.; Kakurai, K.; Honda, Z.; Yamada, K. Magnetic excitations from the singlet dimerized state in Na<sub>2</sub>Co<sub>2</sub>(C<sub>2</sub>O<sub>4</sub>)<sub>3</sub>(H<sub>2</sub>O)<sub>2</sub>. *Phys. Rev. B* **2007**, *75*, 012405. [[CrossRef](#)]
58. Konar, S.; Zangrando, E.; Drew, M.G.B.; Ribas, J.; Chaudhuri, N.R. Synthesis, structural analysis, and magnetic behaviour of three fumarate bridged coordination polymers: Five-fold interpenetrated diamond-like net of NiII, sheets of NiII and CoII. *Dalton Trans.* **2004**, *2*, 260–266. [[CrossRef](#)]
59. Talismanova, M.O.; Sidorov, A.A.; Novotortsev, V.M.; Aleksandrov, G.G.; Nefedov, S.E.; Eremenko, I.L.; Moiseev, I.I. Unusual transformation of the urea molecule giving rise to the NCO<sup>−</sup> anion as a bridging ligand between two CoII atoms. *Russ. Chem. Bull.* **2001**, *50*, 2251–2253. [[CrossRef](#)]
60. Rueff, J.-M.; Masciocchi, N.; Rabu, P.; Sironi, A.; Skoulios, A. Structure and Magnetism of a Polycrystalline Transition Metal Soap – CoII[OOC(CH<sub>2</sub>)<sub>10</sub>COO](H<sub>2</sub>O)<sub>2</sub>. *Eur. J. Inorg. Chem.* **2001**, *2001*, 2843. [[CrossRef](#)]
61. Rueff, J.-M.; Masciocchi, N.; Rabu, P.; Sironi, A.; Skoulios, A. Synthesis, Structure and Magnetism of Homologous Series of Polycrystalline Cobalt Alkane Mono- and Dicarboxylate Soaps. *Chem.-A Eur. J.* **2002**, *8*, 1813–1820. [[CrossRef](#)]

62. Wei, Y.; Yu, Y.; Sa, R.; Li, Q.; Wu, K. Two cobalt(II) coordination polymers  $[\text{Co}_2(\text{H}_2\text{O})_4(\text{Hbidc})_2]_n$  and  $[\text{Co}(\text{Hbidc})]_n$  ( $\text{Hbidc} = 1\text{H-benzimidazole-5,6-dicarboxylate}$ ): Syntheses, crystal structures, and magnetic properties. *CrystEngComm* **2009**, *11*, 1054–1060. [[CrossRef](#)]
63. Demessence, A.; Rogez, G.; Welter, R.; Rabu, P. Structure and magnetic properties of a new cobalt(II) thiophenedicarboxylate coordination polymer showing unprecedented coordination. *Inorg. Chem.* **2007**, *46*, 3423–3425. [[CrossRef](#)] [[PubMed](#)]
64. Fomina, I.G.; Sidorov, A.A.; Aleksandrov, G.G.; Zhilov, V.; Ikorskii, V.N.; Novotortsev, V.M.; Eremenko, I.L.; Moiseev, I.I. Unsymmetrical dinuclear cobalt and nickel trimethylacetate complexes. *Russ. Chem. Bull.* **2004**, *53*, 118–126. [[CrossRef](#)]
65. Brown, D.A.; Errington, W.; Glass, W.K.; Haase, W.; Kemp, T.J.; Nimir, H.; Ostrovsky, S.; Werner, R. Magnetic, Spectroscopic, and Structural Studies of Dicobalt Hydroxamates and Model Hydrolases. *Inorg. Chem.* **2001**, *40*, 5962–5971. [[CrossRef](#)] [[PubMed](#)]
66. Ostrovsky, S.; Werner, R.; Brown, D.A.; Haase, W. Magnetic properties of dinuclear cobalt complexes. *Chem. Phys. Lett.* **2002**, *353*, 290–294. [[CrossRef](#)]
67. Turpeinen, U.; Hämäläinen, R.; Reedijk, J. The dinuclear unit  $\mu$ -aqua-bis( $\mu$ -carboxylato)dimetal. X-ray structure and magnetism of cobalt and nickel(II) compounds containing bridging carboxylato groups and a bridging water molecule. *Polyhedron* **1987**, *6*, 1603–1610. [[CrossRef](#)]
68. Pruchnik, F.P.; Dawid, U.; Kochel, A. Structure and properties of the dinuclear complex  $[\text{Co}_2(\mu\text{-OAc})_2(\text{OAc})_2(\mu\text{-H}_2\text{O})(\text{phen})_2]$ . *Polyhedron* **2006**, *25*, 3647–3652. [[CrossRef](#)]
69. Manna, S.C.; Zangrando, E.; Ribas, J.; Chaudhuri, N.R. Cobalt(ii)–(dpyo)–dicarboxylate networks: Unique H-bonded assembly and rare bridging mode of dpyo in one of them [dpyo = 4,4'-dipyridyl N, N'-dioxide]. *J. Chem. Soc. Dalton Trans.* **2007**, *14*, 1383–1391. [[CrossRef](#)] [[PubMed](#)]
70. Nakagawa, Y.; Kashiwagi, T.; Yamaguchi, H.; Kimura, S.; Honda, Z.; Yamada, K.; Kindo, K.; Hagiwara, M. High Field ESR and Magnetization in  $\text{Na}_2\text{Co}_2(\text{C}_2\text{O}_4)_3(\text{H}_2\text{O})_2$ . *J. Phys. Soc. Jpn.* **2006**, *75*, 124708. [[CrossRef](#)]
71. Price, D.J.; Powell, A.K.; Wood, P.T. Hydrothermal synthesis, structure, stability and magnetism of  $\text{Na}_2\text{Co}_2(\text{C}_2\text{O}_4)_3(\text{H}_2\text{O})_2$ : A new metal oxalate ladder. *J. Chem. Soc. Dalton Trans.* **2000**, *20*, 3566–3569. [[CrossRef](#)]
72. Honda, Z.; Katsumata, K.; Kikkawa, A.; Yamada, K. Thermodynamic Properties in the Approach to the Quantum Critical Point of the Spin-Ladder Material  $\text{Na}_2\text{Co}_2(\text{C}_2\text{O}_4)_3(\text{H}_2\text{O})_2$ . *Phys. Rev. Lett.* **2005**, *95*, 087204. [[CrossRef](#)]
73. Lazarov, N.; Spasojević, V.; Kusigerski, V.; Matić, V.; Milic, M. Magnetic susceptibility calculation of the dinuclear cobalt complex  $6\text{Co}_2(\text{ox})\text{tpmc}_9(\text{ClO}_4)_2\text{a}_3\text{H}_2\text{O}$ . *J. Magn. Magn. Mater.* **2004**, *272*, 1065–1066. [[CrossRef](#)]
74. Lazarov, N.D.; Spasojević, V.; Matic, V.M.; Kusigerski, V.; Guillot, M. Magnetic properties of asymmetric Co ( II ) dimer at low temperatures. *Rev. Roum. Chim.* **2007**, *52*, 1027–1031.
75. Banerjee, A.; Banerjee, S.; Garcia, C.J.G.; Benmansour, S.; Chattopadhyay, S. Field-induced single molecule magnet behavior of a dinuclear cobalt(ii) complex: A combined experimental and theoretical study. *Dalton Trans.* **2020**, *49*, 16778–16790. [[CrossRef](#)]
76. Herchel, R.; Dvořák, Z.; Trávníček, Z.; Mikuriya, M.; Louka, F.R.; Mautner, F.A.; Massoud, S.S. Cobalt(II) and copper(II) covalently and non-covalently dichlorido-bridged complexes of an unsymmetrical tripodal pyrazolyl-pyridyl amine ligand: Structures, magnetism and cytotoxicity. *Inorg. Chim. Acta* **2016**, *451*, 102–110. [[CrossRef](#)]
77. Rajnák, C.; Titiš, J.; Miklovič, J.; Kostakis, G.E.; Fuhr, O.; Ruben, M.; Boča, R. Five mononuclear pentacoordinate Co(II) complexes with field-induced slow magnetic relaxation. *Polyhedron* **2017**, *126*, 174–183. [[CrossRef](#)]
78. Świtlicka, A.; Machura, B.; Penkala, M.; Bieńko, A.; Bieńko, D.C.; Titiš, J.; Rajnák, C.; Boča, R.; Ozarowski, A. Slow magnetic relaxation in hexacoordinated cobalt(ii) field-induced single-ion magnets. *Inorg. Chem. Front.* **2020**, *7*, 2637–2650. [[CrossRef](#)]
79. Gómez-Coca, S.; Urtizbera, A.; Cremades, E.; Alonso, P.J.; Camón, A.; Ruiz, E.; Luis, F. Origin of slow magnetic relaxation in Kramers ions with non-uniaxial anisotropy. *Nat. Commun.* **2014**, *5*, 4300. [[CrossRef](#)]
80. Haldane, F.D.M. O(3) nonlinear model and the topological distinction between integer- and half-integer-spin antiferromagnets in two dimensions. *Phys. Rev. Lett.* **1988**, *61*, 1029–1032. [[CrossRef](#)]
81. Dagotto, E.; Rice, T.M. Surprises on the Way from One- to Two-Dimensional Quantum Magnets: The Ladder Materials. *Science* **1996**, *271*, 618–623. [[CrossRef](#)]
82. Aristov, D.N.; Brünger, C.; Assaad, F.F.; Kiselev, M.N.; Weichselbaum, A.; Capponi, S.; Alet, F. Asymmetric spin-1/2 two-leg ladders: Analytical studies supported by exact diagonalization, DMRG, and Monte Carlo simulations. *Phys. Rev. B Condens. Matter Mater. Phys.* **2010**, *82*, 1–16. [[CrossRef](#)]
83. Shelton, D.; Nersisyan, A. Antiferromagnetic spin ladders: Crossover between spin  $S=1/2$  and  $S=1$  chains. *Phys. Rev. B-Condens. Matter Mater. Phys.* **1996**, *53*, 8521–8532. [[CrossRef](#)] [[PubMed](#)]
84. *CrysAlis RED*; Version 1.171.36.32; Oxford Diffraction Ltd.: Abingdon, UK, 2003.
85. Sheldrick, G.M. SHELXT—Integrated space-group and crystal-structure determination. *Acta Crystallogr. Sect. A Found. Adv.* **2015**, *71*, 3–8. [[CrossRef](#)] [[PubMed](#)]
86. Cazacu, M.; Marcu, M.; Vlad, A.; Caraiman, D.; Racles, C. Synthesis of functional telechelic polydimethylsiloxanes by ion-exchangers catalysis. *Eur. Polym. J.* **1999**, *35*, 1629–1635. [[CrossRef](#)]